Spatiotemporal Tracking of Ocean Current Field With Distributed Acoustic Sensor Network

Ying Zhang, Huifang Chen, *Member, IEEE*, Wen Xu, *Senior Member, IEEE*, T. C. Yang, and Jiamin Huang

***Abstract*—A distributed networked underwater sensor (DNUS) system can provide ocean measurements over a wide area with a large number of sensors. This paper studies the estimation of the ocean current field observed by a DNUS system. Considering that the current field is correlated in time and space, we present a statistically-based acoustic travel time difference tomography method based on a Kalman filter (KF) to reconstruct and track the ocean current field. A spatiotemporal autoregressive (AR) model is used to describe the time evolution of the current field. In the spatiotemporal AR model, the observation region is divided into subtriangle grids. The subtriangles are partitioned into clusters and each cluster is assigned with one AR coefficient. Moreover, the AR coefficients are updated adaptively with the past estimated current velocities. The proposed method is verified with the synthetic observational data generated by a barotropic ocean model. Compared with the regular distributed processing method, the proposed ocean current field reconstruction and tracking method achieves a lower region-integrated root-mean-square error (RMSE). In addition, by making use of the spatiotemporal correlation, the proposed method is robust to the measurement link failure and burst errors in the DNUS system.**

***Index Terms*—Distributed networked underwater sensors (DNUS), ocean current field estimation, spatiotemporal autoregressive model, Kalman filter.**

I. Introduction

SINCE climate change is regarded as a great threat to our living place, ocean state monitoring has begun to attract considerable attention from the environmental scientists. As an important component, ocean current is monitored for port operation, coastal environmental monitoring, offshore exploration, and other commercial and academic purposes. Acoustic Doppler current profiler (ADCP) can measure both directional waves and current profilers. It achieves highly accurate measurements in a limited region. Satellite remote sensing techniques, employing active or passive optical, thermal, and microwave signals, are used for remote monitoring and quantitative mapping of real-time ocean surface field. However, electromagnetic remote sensing can hardly be used for measurements of deep ocean currents [1].

Manuscript received November 12, 2015; revised March 22, 2016; accepted June 6, 2016. Date of publication October 5, 2016; date of current version July 12, 2017. This work was supported in part by the National Natural Science Foundation of China under Grants 41376104 and 61531017, and by the Fundamental Research Funds for the Central Universities.

Associate Editor: Z.-H. Michalopoulou.

The authors are with the College of Information Science and Electronic Engineering, Zhejiang University, Hangzhou 310027, China (e-mail: zhangying@zju.edu.cn; chenhf@zju.edu.cn; wxu@zju.edu.cn; tcyang@zju.edu.cn; hjm818@zju.edu.cn).

Digital Object Identifier 10.1109/JOE.2016.2582018

The ocean is almost transparent to low-frequency sound. The acoustic signal can travel in water for a long distance. Moreover, travel time or some other measurements of an acoustic signal are functions of ocean parameters, such as current velocity, temperature, and so on. Indeed, acoustic waves have been the most effective carriers to probe the ocean body.

Ocean acoustic tomography (OAT), proposed by Munk and Wunsch in 1979, is a classical method employed to measure ocean environmental changes [2]. The purpose of OAT is to infer the state of ocean from the measured travel time or other properties of acoustic transmission [3], [4]. Fig. 1(a) shows the topology of a typical OAT system, where the sensors are usually placed exterior of the studied area.

As an application of OAT in the coastal region, coastal acoustic tomography (CAT) was intended to monitor spatial structure of sound speed or current velocity in the semi-enclosed sea, such as bays, straits, harbors, etc. [5]–[7]. It has been the focus of OAT-related research in recent years due to its capability of continuous environmental monitoring without disturbing shipping traffic and fishing activity.

Distributed networked underwater sensing (DNUS) is an emerging technology, and has attracted great attention as the networking concept and technology mature gradually in the underwater world [8]–[11]. A DNUS system consists of a large number of sensor nodes that are deployed in a specific area to perform a collaborative monitoring task. The sensor configuration of a DNUS system is depicted in Fig. 1(b). With the advent of small, inexpensive, low-power sensor technology, a large number of sensors can be placed in a wide area for sensing, observation, and target detection. Moreover, the sensors can be deployed by the ship within one or two days, saving the cost and time of at-sea operation.

Some existing DNUS systems were presented to estimate the current or temperature field [8], [12]. In [8], a distributed processing method with a DNUS system was proposed to reduce computational complexity. In distributed sensing as well as in OAT, individual data snapshots and the associated parameter estimation are often treated as independent from each other. But in reality, the ocean parameters are time evolving based on the underlying ocean physics. Previous work has shown that a Kalman filter can be adopted to improve the measurement uncertainties in OAT [13], [14]. A Kalman filter will be adopted in this paper for distributed processing.

Park *et al.* assimilated CAT data into a barotropic ocean model using a Kalman filter [15]. Howe *et al.* applied tomography to the ionosphere problem [16], and a Kalman filter was used to assimilate the data into a simple time-dependent model. In OAT,

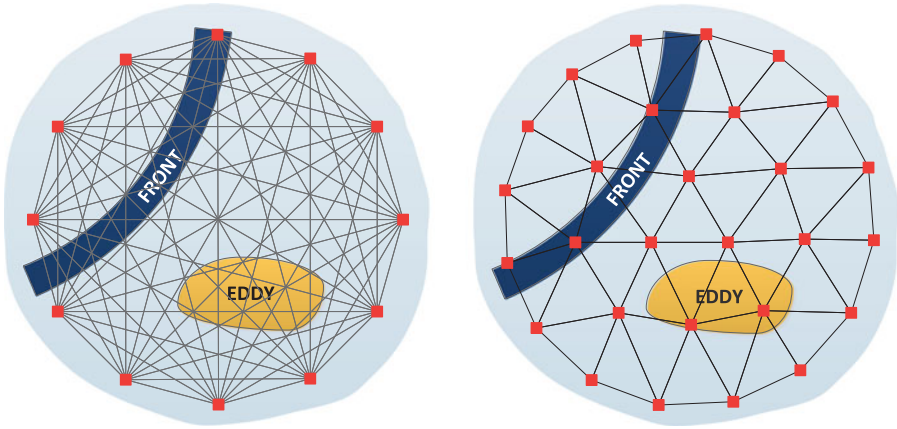

(a) (b)

Fig. 1. Comparison of the sensor configurations of (a) OAT and (b) DNUS system [8]. The squares indicate the sensor nodes and the solid lines represent the acoustic paths.

the sound speed and currents are expressed in terms of a stream function represented by a (truncated) Fourier series. The Kalman filter is applied to the coefficients of the series using a simple temporal persistence (coherence length) [17], implying that the fields with different wavelengths evolve with time with the same rate. In this paper, the Kalman filter is applied directly to the observable current field, taking into consideration its temporal and spatial correlations [18]. Spatial and temporal correlations are observed in real data as well as the current field generated in a simulated ocean model (see Section IV). Moreover, a (2-D) spatiotemporal autoregressive (AR) model [19] is used to describe the time evolution of the current field, in contrast to the aforementioned work where the Kalman filter is represented by a (1-D) temporal AR model. An analysis below will show that the modeling/estimation error is significantly reduced using the spatiotemporal AR model versus the temporal only AR model. Besides, the AR coefficients in this work are adaptively updated using the past and current estimated velocities versus previous work assuming a time-invariant value. Finally, we find an added advantage for a DNUS system, namely that the proposed method is robust against the burst errors and link failure which are common in the underwater acoustic channel. The link failure is more critical to a traditional OAT system which employs fewer nodes than a DNUS system.

In the distributed network, the region can be divided into nonoverlapped subtriangles bounded by the acoustic travel paths. The current field is parameterized by the velocities of the individual subtriangles. The measurement vector includes all the travel time differences of ray paths. Based on the travel time differences, one can map out the current field directly as shown in [8]. This distributed processing method in [8] will be referred to, for simplicity, as the DP method. In this paper, a linear state–space model is incorporated with the state initialized by the initial estimated mean velocity field. An AR model is used to capture the evolution of the state, namely the time-varying horizontal (depth-averaged) ocean current field, where the AR coefficients are updated timely using the estimated states in the past and current time. Two methods are used to compare their tracking (error) performance. The TE–KF method uses the time-evolving Kalman filter (based on the 1-D time-evolving AR model). The STE–KF method uses the spatiotemporal evolution Kalman filter (based on the 2-D spatiotemporal AR model). The effectiveness of the proposed approach is evaluated with the synthetic data generated from the regional ocean modeling system (ROMS) [20].

The rest of the paper is organized as follows. The theoretical foundation of current field estimation and some existing inversion methods are reviewed in Section II. In Section III, the linear dynamic model and the Kalman filter are first reviewed. Then, a time-evolving current field tracking method is proposed. In Section IV, the simulation environment is presented. The proposed tracking method is compared with the ground truth in several situations and the results are discussed. A conclusion is given in Section V.

II. Preliminaries and Problem Formulation

In this section, we define the problem of acoustic current field estimation and introduce some existing inversion approaches based on one snapshot of data.

A. Travel Time Tomography in Horizontal Plane

We focus on ocean current estimation with measured acoustic travel time data in the horizontal plane with a scale of roughly 10 km $\times$ 10 km. In reality, ray paths are reflected by sea surface and bottom in shallow-water environment. Here, a depth-averaged current field is considered, and the complicated ray paths are processed by projecting onto the horizontal plane.

Reconstruction of the ocean current utilizes the fact that the travel time of an acoustic wave propagating from a source to a receiver is a function of both the sound speed and current velocity [21]. Define the travel time difference Δt_{ij} for the reciprocal transmission between two sensor nodes as $\Delta t_{\mathrm{ij}} \equiv (t_{\mathrm{ij}} - t_{\mathrm{ji}})/2$, where t_{ji} is the one-way travel time from nodes i to j. For a nonuniform current field, the travel time difference Δt_{ij} is given by

$$\Delta t_{\mathrm{ij}} = \frac{1}{2}\int_{\mathbf{p}_i}^{\mathbf{p}_j}\left(\frac{1}{c(\mathbf{p})+\mathbf{v}(\mathbf{p})\cdot\mathbf{u}_{\mathrm{ij}}} - \frac{1}{c(\mathbf{p})-\mathbf{v}(\mathbf{p})\cdot\mathbf{u}_{\mathrm{ij}}}\right)\mathrm{d}\mathbf{p} \approx -\int_{\mathbf{p}_i}^{\mathbf{p}_j}\frac{\mathbf{v}(\mathbf{p})\cdot\mathbf{u}_{\mathrm{ij}}}{c^2(\mathbf{p})}\mathrm{d}\mathbf{p} \quad (1)$$

where $\mathbf{p}_i$ is the location of node i, $\mathbf{v}(\mathbf{p})$ is the current vector at location $\mathbf{p}$, $\mathbf{u}_{\rm ij}$ is a unit vector along the path from nodes i to j, and $c(\mathbf{p})$ is the sound speed in water at location $\mathbf{p}$. The sound path is assumed to be overlapped for the reciprocal way. The approximation in (1) requires that the magnitude of the inner product between $\mathbf{v}(\mathbf{p})$ and $\mathbf{u}_{\rm ij}$ is much less than $c(\mathbf{p})$.

Given that the salinity variation is small, the sound speed is mainly determined by the temperature. In this paper, the sound speed is assumed to be constant in the area. Our objective is to reconstruct the horizontal current field with the travel time difference data between node pairs in a DNUS system.

Since travel time difference is used as the measurement in the ocean current tomography, time synchronization among nodes is crucial to the estimation result. Clock synchronization error can be classified into two categories. One is clock jitter, which is random variation of the errors around the zero mean. The other is clock drift, which is the synchronization bias of the errors increasing with time. In this paper, clock jitter is modeled as random measurement noise. However, the related problems caused by clock drift are not considered and remain to be discussed further.

B. Current Field Estimation With Distributed Sensor Network

A key aspect of the estimation problem is how to parameterize the horizontal current field. For the OAT systems, a typical way is to use a so-called stream function [22] which can be represented as a truncated Fourier series. The objective is to solve for the Fourier coefficients so as to obtain the current field distribution. Due to the large number of unknown coefficients, the dimension in this problem is high.

For a DNUS system, the sensor nodes are approximately uniformly distributed in the region, as shown in Fig. 1(b). Each node only communicates with its neighboring nodes. It is shown in [8] that a DNUS system consumes less energy compared with an OAT system at the same frequency due to the short node distances.

To estimate the current field, similar approaches for traditional OAT can be applied in a distributed network [8]. To reduce the computational complexity for solving the inverse problem, a DP method was proposed in [8]. It makes use of the topology of a distributed network by dividing the region into triangular grids. By doing that, the estimation can be performed in a local area with simplified calculation.

Consider a DNUS system with N_s sensor nodes. A travel path is formed by connecting two neighboring nodes. The whole region can be divided into many nonoverlapping triangles by individual travel paths. Let $\Delta_{\{\rm num1,num2,num3\}}$ denote a certain triangle in the network, where $\rm num1$, $\rm num2$, $\rm num3$ are three vertex node indexes of the triangle. By interconnecting the midpoints of three edges, each triangle can be partitioned into four subtriangles. We use Δ with a lowercase letter subscript to represent a subtriangle, such as Δ_a, or we use $\Delta_{\{\rm num1,num2,num3\},a}$ to indicate a specific subtriangle Δ_a in $\Delta_{\{\rm num1,num2,num3\}}$. The set of all the triangles in the region can be denoted as $\mathcal{T}$ with $|\mathcal{T}| = N_{\rm Tri}$, where $|\cdot|$ represents the number of elements in the set.

Fig. 2 shows an example of a distributed sensor network with $N_s = 12$ nodes. The region can be divided into $N_{\rm Tri} = 14$ nonoverlapping triangles. Consider the triangle with three nodes denoted by 1, 2, and 3. The triangle can be partitioned into four subtriangles $\Delta_a, \Delta_b, \Delta_c$, and Δ_d. The current vectors $\mathbf{v}(\Delta_a), \mathbf{v}(\Delta_b)$, and $\mathbf{v}(\Delta_c)$ at the centroids of subtriangles $\Delta_a, \Delta_b, \Delta_c$ are related to the measurement data by (ignoring the noise)

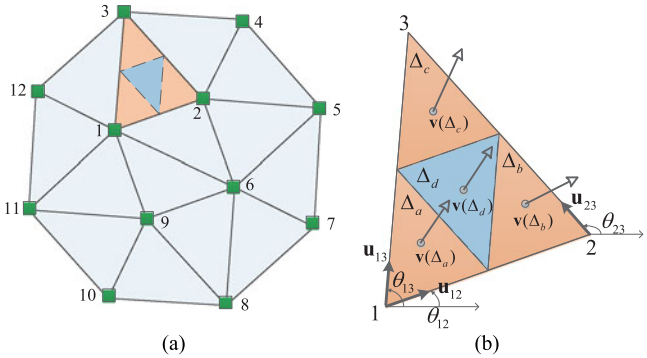

Fig. 2. (a) A distributed sensor network with 12 nodes. (b) One of the triangles in the network with vertexes 1, 2, and 3, which can be partitioned into four subtriangles $\Delta_a, \Delta_b, \Delta_c$, and Δ_d.

$$\Delta t_{13} = \frac{t_{13} - t_{31}}{2} = -\frac{s_{13}}{c_0^2}\frac{\mathbf{v}(\Delta_a)\cdot\mathbf{u}_{13} + \mathbf{v}(\Delta_c)\cdot\mathbf{u}_{13}}{2}$$
$$\Delta t_{12} = \frac{t_{12} - t_{21}}{2} = -\frac{s_{12}}{c_0^2}\frac{\mathbf{v}(\Delta_a)\cdot\mathbf{u}_{12} + \mathbf{v}(\Delta_b)\cdot\mathbf{u}_{12}}{2}$$
$$\Delta t_{23} = \frac{t_{23} - t_{32}}{2} = -\frac{s_{23}}{c_0^2}\frac{\mathbf{v}(\Delta_b)\cdot\mathbf{u}_{23} + \mathbf{v}(\Delta_c)\cdot\mathbf{u}_{23}}{2} \quad (2)$$

where $s_{\rm ij}$ is the distance between nodes i and j, and c_0 is the sound speed.

Assuming that the spatial variation of the current is much smaller than the current itself, the current $\mathbf{v}(\Delta_a) = [v^x(\Delta_a), v^y(\Delta_a)]^T$ is obtained by solving (2) as

$$\hat{v}^x(\Delta_a) = \frac{c_0^2(s_{13}\sin\theta_{13}\Delta t_{12} - s_{12}\sin\theta_{12}\Delta t_{13})}{s_{12}s_{13}\sin(\theta_{12} - \theta_{13})}$$
$$\hat{v}^y(\Delta_a) = \frac{c_0^2(s_{12}\cos\theta_{12}\Delta t_{13} - s_{13}\cos\theta_{13}\Delta t_{12})}{s_{12}s_{13}\sin(\theta_{12} - \theta_{13})} \quad (3)$$

where $\theta_{\rm ij}$ is the angle between $\mathbf{u}_{\rm ij}$ and the unit vector in x-direction, $\hat{v}^x(\Delta_a)$ and $\hat{v}^y(\Delta_a)$ are the estimates of $v^x(\Delta_a)$ and $v^y(\Delta_a)$, respectively, and $(\cdot)^T$ represents the matrix or vector transpose. $\mathbf{v}(\Delta_b)$ and $\mathbf{v}(\Delta_c)$ can be obtained in a similar way.

Applying linear interpolation, $\mathbf{v}(\Delta_d)$ is given by

$$\hat{\mathbf{v}}(\Delta_d) = \frac{\hat{\mathbf{v}}(\Delta_a) + \hat{\mathbf{v}}(\Delta_b) + \hat{\mathbf{v}}(\Delta_c)}{3}. \quad (4)$$

Since the equation sets of the triangles are mutually uncoupled, the DP method can be solved in each triangle individually. As for the current velocities at other locations of the region, a linear interpolation approach can be applied. After that, the current field of the whole region is obtained.

In the DP method, currents can be constructed locally based on data from neighboring nodes, which avoids solving a high-dimensional inverse problem. It is shown in [8] that the DP

method obtains similar results as the conventional tomographic approaches.

In the DP method as well as in OAT [22], individual data snapshots and the associated parameter estimation are treated as independent from each other. That is, the estimation at preceding steps has no effect on the present estimation. However, this is not sufficient in the estimation of ocean current field considering the ocean dynamics. Furthermore, the acoustic channel may be affected by adverse ocean conditions, which will cause transmission loss or suddenly occurred measured noise.

To deal with those practical problems, the estimation should make use of the physical evolution characteristics of the ocean current. Furthermore, the algorithm should be robust to the link failures and burst errors of the received signal. How to model the variance of the ocean current and solve the dynamical equations are the key aspects to be studied in this paper.

III. Current Field Tracking in Distributed Network

In this section, the state–space model and the Kalman filter are first reviewed. Then, in Section III-C, a time-evolving model is formed; in Section III-D, the current field is modeled as evolving with both time and space.

A. State–Space Model

A state–space model is defined by two equations

$$\mathbf{x}_{k+1} = \mathbf{f}_k(\mathbf{x}_k) + \mathbf{w}_k \tag{5}$$

$$\mathbf{z}_k = \mathbf{h}_k(\mathbf{x}_k) + \mathbf{n}_k \tag{6}$$

where k is the discrete time index, $\mathbf{x}_k$ and $\mathbf{z}_k$ are the state vector and measurement vector, respectively, and $\mathbf{w}_k$ and $\mathbf{n}_k$ are the state noise and the measurement noise, respectively. $\mathbf{f}_k$ is the state transition function which illustrates the state evolution from k to $k+1$, $\mathbf{h}_k$ is the measurement function which maps the state space into the observation space.

When $\mathbf{f}_k$ and $\mathbf{h}_k$ are both linear, (5) and (6) can be formulated as

$$\mathbf{x}_{k+1} = \mathbf{F}_k\mathbf{x}_k + \mathbf{w}_k \tag{7}$$

$$\mathbf{z}_k = \mathbf{H}_k\mathbf{x}_k + \mathbf{n}_k \tag{8}$$

where $\mathbf{F}_k$ is the state transition matrix, and $\mathbf{H}_k$ is the measurement matrix.

Given a dynamic system with a collection of state measurements up to the current time, the filtering problem aims at computing the optimal estimate of the state. This involves iteratively updating the state estimate once a new measurement is available, yielding a so-called sequential estimation scheme.

B. Kalman Filter

The Kalman filter is one of the most well-known sequential estimation algorithms. In terms of minimizing the mean square error (MSE), it is optimal for a linear system with Gaussian white process and measurement noise.

In (7) and (8), $\mathbf{w}_k$ and $\mathbf{n}_k$ are assumed to be stationary zero mean Gaussian white noise processes with respective covariance matrices $\mathbf{Q}_k$ and $\mathbf{R}_k$. Let $\hat{\mathbf{x}}_k$ and $\bar{\mathbf{x}}_k$ be the estimate and predict of $\mathbf{x}_k$, and define $\mathbf{e}_k = \hat{\mathbf{x}}_k - \mathbf{x}_k$ and $\bar{\mathbf{e}}_k = \bar{\mathbf{x}}_k - \mathbf{x}_k$ as the estimate and predict errors, respectively. The error covariance matrices of $\hat{\mathbf{x}}_k$ and $\bar{\mathbf{x}}_k$ can be expressed by

$$\mathbf{M}_k = E\left(\mathbf{e}_k\mathbf{e}_k^T\right) \tag{9}$$

$$\mathbf{P}_k = E\left(\bar{\mathbf{e}}_k\bar{\mathbf{e}}_k^T\right) \tag{10}$$

where $E(\cdot)$ represents the mathematical expectation.

The objective is to obtain estimate $\hat{\mathbf{x}}_k$ of state $\mathbf{x}_k$ from measurement $\mathbf{z}_k$ so as to minimize the MSE $\mathrm{tr}(\mathbf{M}_k)$, where $\mathrm{tr}(\cdot)$ is the trace operation. The Kalman filter can be expressed in two steps as follows.

Update:

$$\hat{\mathbf{x}}_k = \bar{\mathbf{x}}_k + \mathbf{K}_k(\mathbf{z}_k - \mathbf{H}_k\bar{\mathbf{x}}_k) \tag{11}$$

$$\mathbf{K}_k = \mathbf{P}_k\mathbf{H}_k^T(\mathbf{R}_k + \mathbf{H}_k\mathbf{P}_k\mathbf{H}_k^T)^{-1} \tag{12}$$

$$\mathbf{M}_k = \mathbf{P}_k - \mathbf{K}_k\mathbf{H}_k\mathbf{P}_k. \tag{13}$$

Forecast:

$$\mathbf{P}_{k+1} = \mathbf{F}_k\mathbf{M}_k\mathbf{F}_k^T + \mathbf{Q}_k \tag{14}$$

$$\bar{\mathbf{x}}_{k+1} = \mathbf{F}_k\hat{\mathbf{x}}_k. \tag{15}$$

C. Temporal Evolution Tracking of Current Field (TE–KF)

The physical process in ocean observations often evolves sequentially in time or space [23]. In this section, we develop a time-evolving model of the current field. This concept was first studied in [24], where the velocity in each subtriangle is modeled as a Gaussian random walk process. In [25], an AR model was used to predict the velocity of the littoral current and wave direction of a fixed position. In this section, the variation of the velocity is modeled as a temporal AR process so as to track the current evolution over time. For simplicity, a first-order AR model is utilized. The Kalman filter is used to solve the state–space model problem. Hence, this method is named as temporal evolution Kalman filter (TE–KF).

1) State Evolution Process: For temporal evolution tracking, the state–space model is employed in each triangle individually.

Consider one triangle in Fig. 2, for example, $\Delta_{\{1,2,3\}}$. In this triangle, four uncoupled local state transition equations are built. The local state vectors of those equations are chosen as the current velocities of subtriangles $\Delta_a, \Delta_b, \Delta_c$, and Δ_d, respectively. For example, for subtriangle Δ_a, the local state vector is $\mathbf{x}_{k,\Delta_a} = [\mathbf{v}_k(\Delta_a)] = [v_k^x(\Delta_a), v_k^y(\Delta_a)]^T$.

To incorporate time-evolving characteristics of the current field, the velocity component in x- or y-direction of each subtriangle is modeled as a first-order AR process. The local state transition equation for subtriangle Δ_a is given by

$$\mathbf{v}_{k+1}(\Delta_a) = \mathbf{\Lambda}_k^{\gamma}\mathbf{v}_k(\Delta_a) + \boldsymbol{\omega}_k(\Delta_a) \tag{16}$$

where $\mathbf{\Lambda}_k^{\gamma} = \mathrm{diag}(\gamma_k^x, \gamma_k^y)$ is a 2×2 diagonal, where γ_k^x and γ_k^y are the AR coefficients in x- and y-directions at time k, respectively; and $\boldsymbol{\omega}_k(\Delta_a)$ is the state noise vector of Δ_a.

For Δ_b, Δ_c, and Δ_d, similar state transition equations can be formed.

Let the global state vector and global state noise vector be

$$\mathbf{x}_k = [v_k^x(\Delta_a), v_k^y(\Delta_a), v_k^x(\Delta_b), v_k^y(\Delta_b), \ldots]^T \tag{17}$$

$$\mathbf{w}_k = [\omega_k^x(\Delta_a), \omega_k^y(\Delta_a), \omega_k^x(\Delta_b), \omega_k^y(\Delta_b), \ldots]^T \tag{18}$$

where $\mathbf{x}_k$ includes the velocities of all the subtriangles. Let $\mathcal{S}$ be the set of all the subtriangles in the region with the element number $|\mathcal{S}| = N_{\mathrm{Sub}}$. Since one triangle is divided into four subtriangles $N_{\mathrm{Sub}} = 4N_{\mathrm{Tri}}$. $\mathbf{x}_k$ is a column vector with length $2N_{\mathrm{Sub}}$.

The global state transition model is given by

$$\mathbf{x}_{k+1} = (\mathbf{I}_{N_{\mathrm{Sub}}} \otimes \mathbf{\Lambda}_k^{\gamma})\, \mathbf{x}_k + \mathbf{w}_k \tag{19}$$

where $\mathbf{I}_{N_{\mathrm{Sub}}}$ is an identity matrix of size N_{Sub}, and $\otimes$ denotes the Kronecker product of matrices. To reduce the unknown coefficients, it is assumed that the AR coefficients for each subtriangle in a region are the same.

In (19), an estimate of $\mathbf{\Lambda}_k^{\gamma}$ needs to be acquired. To track the variance of the model, $\mathbf{\Lambda}_k^{\gamma}$ is updated with time. This can be estimated using the Yule–Walker method [26] from some training data (known or past estimated). Here we use the training data $[\hat{\mathbf{x}}_{k-K_{\mathrm{AR}}}, \ldots, \hat{\mathbf{x}}_k]$, which combine the past K_{AR} estimated states and the current estimated state.

2) Measurement Process: To construct measurement equations, the subtriangles can be segmented into two categories: one is the subtriangles located at the vertexes of the triangle, such as Δ_a, Δ_b, and Δ_c in Fig. 2(b), and another is the subtriangles in the center of the triangle, such as Δ_d.

Define $\Delta t_{ij,k}$ as the travel time difference between nodes i and j at time k. For Δ_a, the local measurement vector is chosen as $\mathbf{z}_{k,\Delta_a} = [\Delta t_{13,k}, \Delta t_{12,k}]^T$ because the travel paths from nodes 1 to 3 and from nodes 1 to 2 overlap with two edges of Δ_a. The local measurement equations can be derived from (3), that is

$$\begin{bmatrix} \Delta t_{13,k} \\ \Delta t_{12,k} \end{bmatrix} = \frac{-1}{c_0^2} \begin{bmatrix} s_{13}\cos\theta_{13} & s_{13}\sin\theta_{13} \\ s_{12}\cos\theta_{12} & s_{12}\sin\theta_{12} \end{bmatrix} \begin{bmatrix} v_k^x(\Delta_a) \\ v_k^y(\Delta_a) \end{bmatrix} + \begin{bmatrix} n_k(P_{13}) \\ n_k(P_{12}) \end{bmatrix} \tag{20}$$

where P_{ij} represents the travel path between nodes i and j, and $n_k(P_{\mathrm{ij}})$ is the measurement noise on path P_{ij}. From (20), the local measurement matrix of Δ_a can be written as

$$\mathbf{H}_{k,\Delta_a} = -\frac{1}{c_0^2} \begin{bmatrix} s_{13}\cos\theta_{13} & s_{13}\sin\theta_{13} \\ s_{12}\cos\theta_{12} & s_{12}\sin\theta_{12} \end{bmatrix}. \tag{21}$$

For subtriangle Δ_d, the local measurement vector is $\mathbf{z}_{k,\Delta_d} = [\Delta t_{13,k}, \Delta t_{12,k}, \Delta t_{23,k}]^T$, which involves the time differences of all three travel paths of the triangle. The local measurement matrix of Δ_d is

$$\mathbf{H}_{k,\Delta_d} = -\frac{1}{c_0^2} \begin{bmatrix} s_{13}\cos\theta_{13} & s_{13}\sin\theta_{13} \\ s_{12}\cos\theta_{12} & s_{12}\sin\theta_{12} \\ s_{23}\cos\theta_{23} & s_{23}\sin\theta_{23} \end{bmatrix}. \tag{22}$$

Hence, for each subtriangle in the region, the local measurement matrix can be constructed in a similar way.

The global measurement equations are expressed by

$$\begin{bmatrix} \mathbf{z}_{k,\Delta_a} \\ \mathbf{z}_{k,\Delta_b} \\ \vdots \end{bmatrix} = \begin{bmatrix} \mathbf{H}_{k,\Delta_a} & & \\ & \mathbf{H}_{k,\Delta_b} & \\ & & \ddots \end{bmatrix} \begin{bmatrix} \mathbf{x}_{k,\Delta_a} \\ \mathbf{x}_{k,\Delta_b} \\ \vdots \end{bmatrix} + \begin{bmatrix} \mathbf{n}_{k,\Delta_a} \\ \mathbf{n}_{k,\Delta_b} \\ \vdots \end{bmatrix} \tag{23}$$

where off-diagonal elements are all 0 s for the global measurement matrix.

Since (19) and (23) are linear, the problem can be solved using the Kalman filter with the steps following (11)–(15). A linear interpolation method can then be used to obtain the whole current field.

D. Spatiotemporal Evolution Tracking of Current Field (STE–KF)

In this section, we propose a spatiotemporal current field tracking model.

1) Spatial Correlation: In Section III-C, the current field is considered to be highly correlated in a short time interval. On the other hand, fluids are considered to obey the continuum assumption. Flow velocity is taken to be well defined at infinitesimally small points and vary continuously from one point to another. Since liquid is a nearly incompressible fluid, the flow velocities in liquid are also correlated in space.

To explain the spatial correlation of the current field, a spatial correlation coefficient for velocities at positions $\mathbf{p}_1$ and $\mathbf{p}_2$ is defined as

$$R_k(\mathbf{p}_1, \mathbf{p}_2) = \frac{E_k\left[\mathbf{v}_k(\mathbf{p}_1) \cdot \mathbf{v}_k(\mathbf{p}_2)\right]}{\sqrt{E_k\left[\|\mathbf{v}_k(\mathbf{p}_1)\|^2\right] E_k\left[\|\mathbf{v}_k(\mathbf{p}_2)\|^2\right]}} \tag{24}$$

where $\mathbf{v}_k(\mathbf{p}_1) \cdot \mathbf{v}_k(\mathbf{p}_2)$ is the inner product of velocities $\mathbf{v}_k(\mathbf{p}_1)$ and $\mathbf{v}_k(\mathbf{p}_2)$, and $\|\cdot\|$ represents the Euclidean norm. The spatial correlation depends on both the magnitude and direction of the separation $\mathbf{r} = \mathbf{p}_2 - \mathbf{p}_1$. Here we focus on the variation with the distance $r = \|\mathbf{r}\|$.

To analyze the properties of spatial correlation, we can separate the velocity into streamwise and cross-stream components, which are called the longitudinal and lateral velocities, respectively, as shown in Fig. 3(a). Fig. 3(b) shows the typical correlation curves of the two components [27], [28]. The spatial correlation curve of $\mathbf{v}_k(\mathbf{p}_1)$ and $\mathbf{v}_k(\mathbf{p}_2)$ should be a linear combination of the two curves, which shows high correlation when r is small. This spatial correlation characteristic will be verified with the simulation results in Section IV-D1.

Based on the correlation of the current velocities in time and space, a spatiotemporal AR model can be built, which is used to capture possible temporal and spatial interactions across spatial grids. The spatiotemporal AR model is constructed in the whole region. This is different from the method presented

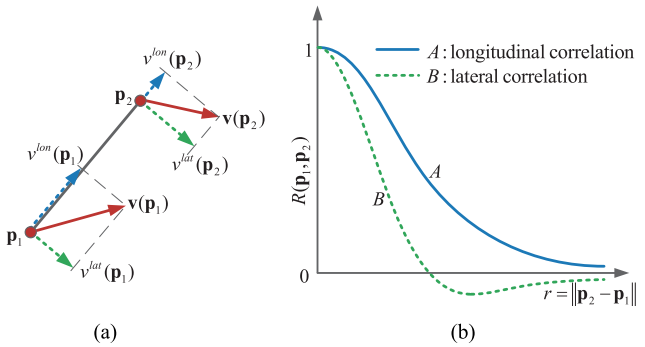

Fig. 3. An interpretation of spatial correlation of turbulence [27]. (a) Schematic representation of velocity components. (b) Typical correlation curves. Curve A stands for the longitudinal correlation and curve B stands for the lateral correlation.

in Section III-C, where the state transition model is conducted in each triangle separately.

2) State Evolution Process: The velocities of all the subtriangles in x- and y-directions form the state vector, which is the same as in (17). The set of all the elements in state vector $\mathbf{x}_k$ is

$$\mathcal{X} = \{\mathbf{v}_k(\Delta_p) \,|\, \Delta_p \in \mathcal{S}\}. \tag{25}$$

All the measured travel time differences between neighboring nodes constitute the set of all the elements in measurement vector as

$$\mathcal{Z} = \{\Delta t_{ij,k} \,|\, P_{\mathrm{ij}} \in \mathcal{P}\} \tag{26}$$

where $\mathcal{P}$ is the set of all the travel paths in the distributed network.

To illustrate the correlations over time and space, the variance of the current field can be represented as a spatiotemporal AR model, which is commonly used to model the evolution of spatial patterns through time [18], [29]. Similar to TE–KF, the order of AR model in time series is 1. Then, the spatiotemporal AR model is expressed as

$$\mathbf{x}_{k+1} = \sum_{m=0}^{M} \left(\mathbf{S}_m \otimes \mathbf{\Lambda}^{\rho}_{m,k}\right) \mathbf{x}_k + \mathbf{w}_k \tag{27}$$

where M is the spatial order, $\mathbf{S}_m$ is the spatial lag operator of spatial order m, satisfying that $\mathbf{S}_0 = \mathbf{I}_{N_{\mathrm{Sub}}}$, and the sum of each row of $\mathbf{S}_m$ equals 1 for $m = 1, \ldots, M$. Martin and Oeppen [18] use rectangle grids in Cartesian coordinates, where the lag operator is clearly defined. For triangles, the lag operator is used to select the triangle with a certain distance (lag) for the current triangle. See (28) for details. $\mathbf{\Lambda}^{\rho}_{m,k} = \mathrm{diag}(\rho^x_{m,k}, \rho^y_{m,k})$ is a 2×2 diagonal coefficient matrix of the mth order at time index k, and $\mathbf{w}_k$ is the disturbance vector.

Depending on the distances to the centroid of the specific subtriangle, the subtriangles in the region can be partitioned into many clusters. The subtriangles in the same cluster are assigned with one AR coefficient. It is shown in Fig. 3(b) that the spatial coefficient decreases as the distance increases. To reduce the number of unknown AR coefficients, the subtriangles with larger distance are not included in the model since the correlation coefficient is smaller. The spatial lag operator $\mathbf{S}_m$ is associated with the subtriangles in cluster m. Next, we introduce an example of three clusters, which means that $M = 2$.

Following (27), the spatiotemporal AR model of the subtriangle Δ_p is

$$\mathbf{v}_{k+1}(\Delta_p) = \mathbf{\Lambda}^{\rho}_{0,k}\mathbf{v}_k(\Delta_p) + \mathbf{\Lambda}^{\rho}_{1,k}\frac{1}{|\mathcal{E}_p|}\sum_{\Delta_{p_i}\in\mathcal{E}_p}\mathbf{v}_k(\Delta_{p_i}) + \mathbf{\Lambda}^{\rho}_{2,k}\frac{1}{|\mathcal{V}_p|}\sum_{\Delta_{p_j}\in\mathcal{V}_p}\mathbf{v}_k(\Delta_{p_j}) + \boldsymbol{\epsilon}_k(\Delta_p) \tag{28}$$

where $\mathbf{\Lambda}^{\rho}_{0,k} = \mathrm{diag}(\rho^x_{0,k}, \rho^y_{0,k})$, $\mathbf{\Lambda}^{\rho}_{1,k} = \mathrm{diag}(\rho^x_{1,k}, \rho^y_{1,k})$ and $\mathbf{\Lambda}^{\rho}_{2,k} = \mathrm{diag}(\rho^x_{2,k}, \rho^y_{2,k})$, $\mathcal{E}_p$ and $\mathcal{V}_p$ are the sets of the subtriangles which share an edge and a vertex with subtriangle Δ_p, respectively, and $\boldsymbol{\epsilon}_k(\Delta_p)$ is the state noise vector of Δ_p.

The subtriangles in the same set are at about the same distances to the centroid of Δ_p. We simplify the notations of (28) by

$$\mathbf{v}_k(\Delta_{p\mathcal{E}}) = \frac{1}{|\mathcal{E}_p|}\sum_{\Delta_{p_i}\in\mathcal{E}_p}\mathbf{v}_k(\Delta_{p_i})$$
$$\mathbf{v}_k(\Delta_{p\mathcal{V}}) = \frac{1}{|\mathcal{V}_p|}\sum_{\Delta_{p_j}\in\mathcal{V}_p}\mathbf{v}_k(\Delta_{p_j}) \tag{29}$$

which represent the average velocities in the subtriangle sets $\mathcal{E}_p$ and $\mathcal{V}_p$, respectively. Then, (28) can be rewritten as

$$\mathbf{v}_{k+1}(\Delta_p) = \mathbf{\Lambda}^{\rho}_{0,k}\mathbf{v}_k(\Delta_p) + \mathbf{\Lambda}^{\rho}_{1,k}\mathbf{v}_k(\Delta_{p\mathcal{E}}) + \mathbf{\Lambda}^{\rho}_{2,k}\mathbf{v}_k(\Delta_{p\mathcal{V}}) + \boldsymbol{\epsilon}_k(\Delta_p). \tag{30}$$

Define $\boldsymbol{\rho}_{0,k} = [\rho^x_{0,k}, \rho^y_{0,k}]$, $\boldsymbol{\rho}_{1,k} = [\rho^x_{1,k}, \rho^y_{1,k}]$ and $\boldsymbol{\rho}_{2,k} = [\rho^x_{2,k}, \rho^y_{2,k}]$ as the time-dependent AR model coefficient vectors for clusters 0, 1, and 2, respectively. The vector including all the AR coefficients is defined as $\boldsymbol{\rho}_k = [\boldsymbol{\rho}_{0,k}, \boldsymbol{\rho}_{1,k}, \boldsymbol{\rho}_{2,k}]$.

Fig. 4 demonstrates an example of adjacent subtriangles and AR coefficient assignment of subtriangle Δ_p for current velocity. For the subtriangle Δ_p, $|\mathcal{E}_p| = 3$ and $|\mathcal{V}_p| = 9$. It should be noted that for the subtriangle which locates at the edge of the region, the number of adjacent subtriangles is less than that in the central part.

To obtain (30), an estimate of $\boldsymbol{\rho}_k$ needs to be acquired. Similar to TE–KF, this can be done using the Yule–Walker method [26] from some past estimated training data.

Specifically, right multiplying both sides of (30) by $\mathbf{v}_k(\Delta_p)$, $\mathbf{v}_k(\Delta_{p\mathcal{E}})$ and $\mathbf{v}_k(\Delta_{p\mathcal{V}})$, respectively, and taking expectations, we have six linear equations with six unknown parameters. The equation sets for x- and y-directions are uncoupled, and they therefore can be solved separately. The matrix form of the equations can be written as (31), shown at the bottom of the next page, where

$$E_{\kappa,p}[\cdot] = \frac{1}{K_{\mathrm{AR}}}\frac{1}{N_{\mathrm{Sub}}}\sum_{\kappa=k-K_{\mathrm{AR}}}^{k-1}\sum_{\Delta p\in\mathcal{S}}[\cdot] \tag{32}$$

is the average in both time and space domains for each element in the matrix. K_{AR} is the length of training data in the past.

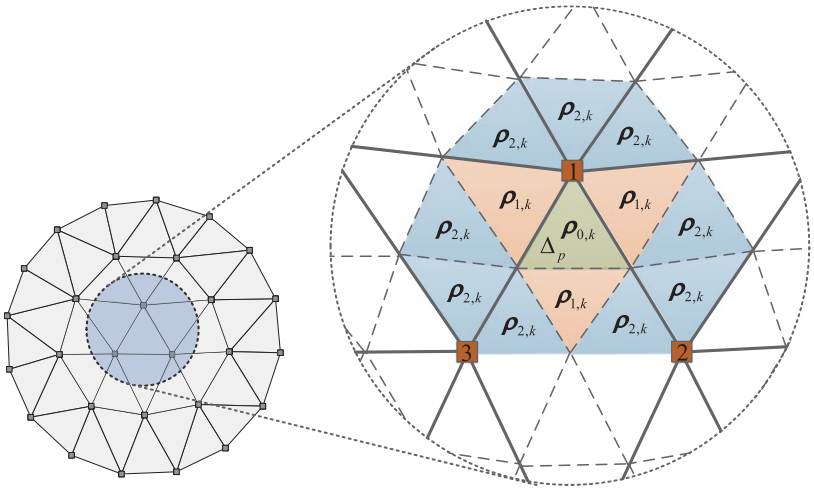

Fig. 4. Spatial region of spatiotemporal AR model for the case of three clusters. The shadowed part shows all the adjacent subtriangles of subtriangle Δ_p at time index k which are related to the state of subtriangle Δ_p at time index $k+1$.

Note that $E_{\kappa,p}\left[\mathbf{v}_\kappa(\Delta_p)\boldsymbol{\epsilon}_\kappa^T(\Delta_p)\right] = E_{\kappa,p}\left[\mathbf{v}_\kappa(\Delta_{p_\mathcal{E}})\boldsymbol{\epsilon}_\kappa^T(\Delta_p)\right] = E_{\kappa,p}\left[\mathbf{v}_\kappa(\Delta_{p_\mathcal{V}})\boldsymbol{\epsilon}_\kappa^T(\Delta_p)\right] = \mathbf{0}$ because the random perturbation is not correlated with the state values of the process. Since (31) is sensitive to the fluctuation, which results in an ill-posed problem, the estimate of AR coefficients in (31), $\hat{\boldsymbol{\rho}}_k = [\hat{\boldsymbol{\rho}}_{0,k}, \hat{\boldsymbol{\rho}}_{1,k}, \hat{\boldsymbol{\rho}}_{2,k}]$, can be obtained with the Tikhonov regularization method [30].

The AR coefficients at time index k can thus be estimated using training data $[\hat{\mathbf{x}}_{k-K_{\mathrm{AR}}}, \ldots, \hat{\mathbf{x}}_k]$, which combine the past K_{AR} estimated states and the current estimated state. As the AR coefficients are time varying, the estimation should be executed in each time index.

The spatial lag operator can be formulated as follows. Define $\mathcal{C}_i^m$ as the set of subtriangles in cluster m for the ith subtriangle. If the jth subtriangle is in cluster m of the ith subtriangle, $\mathbf{S}_m[i,j] = 1/|\mathcal{C}_i^m|$. Otherwise, $\mathbf{S}_m[i,j] = 0$. After $\mathbf{S}_m$ and $\boldsymbol{\Lambda}_{m,k}^\rho$ are obtained, $\mathbf{F}_k$ can be updated using (30).

For the case of two clusters, $\boldsymbol{\rho}_k = [\boldsymbol{\rho}_{0,k}, \boldsymbol{\rho}_{1,k}]$. For four clusters, $\boldsymbol{\rho}_k = [\boldsymbol{\rho}_{0,k}, \boldsymbol{\rho}_{1,k}, \boldsymbol{\rho}_{2,k}, \boldsymbol{\rho}_{3,k}]$, where $\boldsymbol{\rho}_{3,k} = [\rho_{3,k}^x, \rho_{3,k}^y]$ is the coefficient vector assigned for cluster 3. The distances of the subtriangles assigned with $\boldsymbol{\rho}_{3,k}$ to the centroid of Δ_p are almost the same, and are slightly larger than those assigned with $\boldsymbol{\rho}_{2,k}$. The above approach can be generalized in a straightforward way to the case of more clusters.

3) Measurement Process: As stated in (8), the relationship between the state $\mathbf{x}_k$ and the measurement $\mathbf{z}_k$ at time index k is given by $\mathbf{z}_k = \mathbf{H}_k\mathbf{x}_k + \mathbf{n}_k$. The measurement vector $\mathbf{z}_k$ consists of all the travel time difference measurements between neighboring nodes, as shown in (26).

The global measurement matrix $\mathbf{H}_k$ can be constructed based on (21) and (22), which means the travel time difference is related to the current velocities of the subtriangles around the travel path. Define $\mathcal{S}_{\mathrm{ij}}$ as the set of the subtriangles which affect the travel time difference of path P_{ij}, i.e., one edge or vertex of the subtriangles in $\mathcal{S}_{\mathrm{ij}}$ is located at path P_{ij} (not including nodes i and j).

The measurement $\Delta t_{ij,k}$ can be represented as

$$\begin{aligned}\Delta t_{ij,k} &= \frac{-s_{\mathrm{ij}}}{c_0^2}\frac{1}{|\mathcal{S}_{\mathrm{ij}}|}\sum_{\Delta_p\in\mathcal{S}_{\mathrm{ij}}}[\mathbf{v}_k(\Delta_p)\cdot\mathbf{u}_{\mathrm{ij}}] + n_k(P_{\mathrm{ij}}) \\ &= \frac{-s_{\mathrm{ij}}}{c_0^2}\frac{1}{|\mathcal{S}_{\mathrm{ij}}|}\sum_{\Delta_p\in\mathcal{S}_{\mathrm{ij}}}[\cos\theta_{\mathrm{ij}}v_k^x(\Delta_p) + \sin\theta_{\mathrm{ij}}v_k^y(\Delta_p)] \\ &\quad + n_k(P_{\mathrm{ij}}). \end{aligned} \tag{33}$$

As illustrated in Fig. 5, the triangle with vertexes 1, 2, and 3 and the triangle with vertexes 1, 2, and 4 share a travel path P_{12}. In this example, there are six subtriangles in the set $\mathcal{S}_{12}$. One edge of subtriangles $\Delta_{\{1,2,3\},a}, \Delta_{\{1,2,3\},b}, \Delta_{\{1,2,4\},a}, \Delta_{\{1,2,4\},b}$ and one vertex of subtriangles $\Delta_{\{1,2,3\},d}$ and $\Delta_{\{1,2,4\},d}$ are on the path P_{12}. The measurement $\Delta t_{12,k}$ is determined by the current velocities of the subtriangles in the set $\mathcal{S}_{12}$. That is

$$\begin{aligned}\Delta t_{12,k} = \frac{-s_{12}}{6c_0^2}\big[&\mathbf{v}_k(\Delta_{\{1,2,3\},a})\cdot\mathbf{u}_{12} + \mathbf{v}_k(\Delta_{\{1,2,3\},b})\cdot\mathbf{u}_{12} \\ &+ \mathbf{v}_k(\Delta_{\{1,2,3\},d})\cdot\mathbf{u}_{12} + \mathbf{v}_k(\Delta_{\{1,2,4\},a})\cdot\mathbf{u}_{12} \\ &+ \mathbf{v}_k(\Delta_{\{1,2,4\},b})\cdot\mathbf{u}_{12} + \mathbf{v}_k(\Delta_{\{1,2,3\},d})\cdot\mathbf{u}_{12}\big] \\ &+ n_k(P_{12}). \end{aligned} \tag{34}$$

$$\begin{bmatrix} E_{\kappa,p}\left[\hat{\mathbf{v}}_\kappa(\Delta_p)\hat{\mathbf{v}}_\kappa^T(\Delta_p)\right] & E_{\kappa,p}\left[\hat{\mathbf{v}}_\kappa(\Delta_{p_\mathcal{E}})\hat{\mathbf{v}}_\kappa^T(\Delta_p)\right] & E_{\kappa,p}\left[\hat{\mathbf{v}}_\kappa(\Delta_{p_\mathcal{V}})\hat{\mathbf{v}}_\kappa^T(\Delta_p)\right] \\ E_{\kappa,p}\left[\hat{\mathbf{v}}_\kappa(\Delta_p)\hat{\mathbf{v}}_\kappa^T(\Delta_{p_\mathcal{E}})\right] & E_{\kappa,p}\left[\hat{\mathbf{v}}_\kappa(\Delta_{p_\mathcal{E}})\hat{\mathbf{v}}_\kappa^T(\Delta_{p_\mathcal{E}})\right] & E_{\kappa,p}\left[\hat{\mathbf{v}}_\kappa(\Delta_{p_\mathcal{V}})\hat{\mathbf{v}}_\kappa^T(\Delta_{p_\mathcal{E}})\right] \\ E_{\kappa,p}\left[\hat{\mathbf{v}}_\kappa(\Delta_p)\hat{\mathbf{v}}_\kappa^T(\Delta_{p_\mathcal{V}})\right] & E_{\kappa,p}\left[\hat{\mathbf{v}}_\kappa(\Delta_{p_\mathcal{E}})\hat{\mathbf{v}}_\kappa^T(\Delta_{p_\mathcal{V}})\right] & E_{\kappa,p}\left[\hat{\mathbf{v}}_\kappa(\Delta_{p_\mathcal{V}})\hat{\mathbf{v}}_\kappa^T(\Delta_{p_\mathcal{V}})\right] \end{bmatrix} \begin{bmatrix} \hat{\boldsymbol{\Lambda}}_{0,k}^\rho \\ \hat{\boldsymbol{\Lambda}}_{1,k}^\rho \\ \hat{\boldsymbol{\Lambda}}_{2,k}^\rho \end{bmatrix} = \begin{bmatrix} E_{\kappa,p}\left[\hat{\mathbf{v}}_\kappa(\Delta_p)\hat{\mathbf{v}}_{\kappa+1}^T(\Delta_p)\right] \\ E_{\kappa,p}\left[\hat{\mathbf{v}}_\kappa(\Delta_{p_\mathcal{E}})\hat{\mathbf{v}}_{\kappa+1}^T(\Delta_p)\right] \\ E_{\kappa,p}\left[\hat{\mathbf{v}}_\kappa(\Delta_{p_\mathcal{V}})\hat{\mathbf{v}}_{\kappa+1}^T(\Delta_p)\right] \end{bmatrix} \tag{31}$$

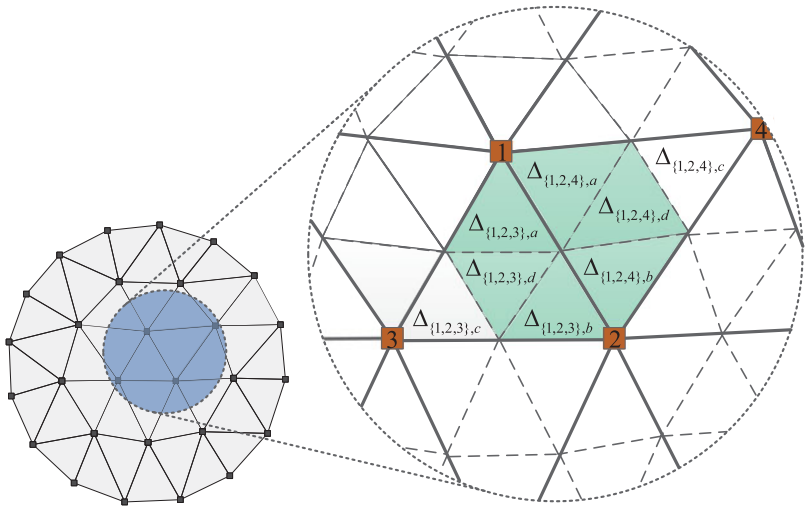

Fig. 5. The relationship between measurement and state. The shadowed subtriangles are involved in the measurement $\Delta t_{12,k}$.

Again, the linear dynamic problem can be solved using the Kalman filter, and a linear interpolation method can be applied to obtain the whole current field. The approach proposed in this section is called the spatiotemporal evolution Kalman filter (STE–KF). The difference with the time-evolving model in Section III-C is that the system is represented by one global state–space model. Hence, the algorithm needs to be executed in the fusion center.

In our method, the idea of spatiotemporal state dynamics is similar to that in [19]. The methodology in [19] discretizes the investigation area into square grids in which the velocity is assumed to be constant. Also, the rays connect all pairs of transmitters and receivers. In contrast, the triangular grid division here is based on the travel paths of the distributed sensor nodes, which makes use of the topology of the DNUS system and results in a linear state–space model. Moreover, the order of the spatiotemporal AR model in our proposed method can be adjusted. We also allow AR coefficients to change with time and show how to update the time-varying AR coefficients.

In the underwater environment, the transmission link may fail due to the complexity of the underwater channel. Measurement failure can be discovered by the system when the detected peak of the signal correlation is missed or occurs in an unreasonable location.

Also, the measurement may be affected by the interference such as noise from the ship and so on. This will result in a burst error of the measurement. The burst error can be viewed as an increase of the measurement error. When the burst error occurs, the signal-to-noise ratio (SNR) of the received signal may decrease, which is similar to the situation of link failure. One can modify the measurement noise according to the received SNR. That relies on whether the signal and the burst noise can be separated at least for part of the time.

IV. Simulation Evaluations

In this section, we validate the proposed method by extensive simulations. First, the method of generating synthetic data used

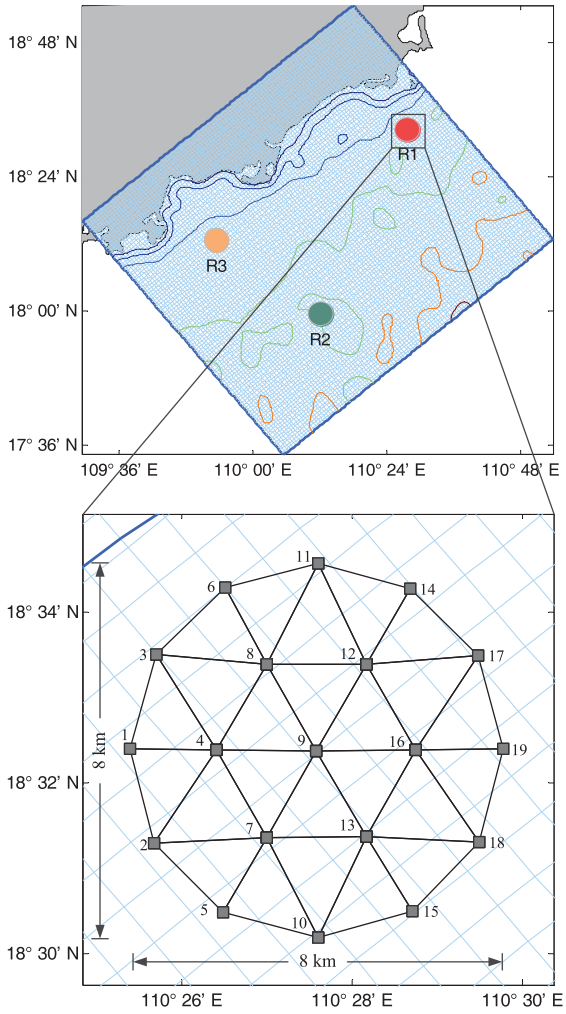

Fig. 6. The upper figure shows the model grid and bathymetry of the model domain. The region is in northwest of the South China Sea. The colored circles indicate the observation regions R1, R2, and R3. The contour lines are the water depths of 10, 20, 50, 100, 150, and 200 m. The bottom figure shows the observation region and the topology of the network with $N_s = 19$ sensors. The black squares represent the sensor nodes.

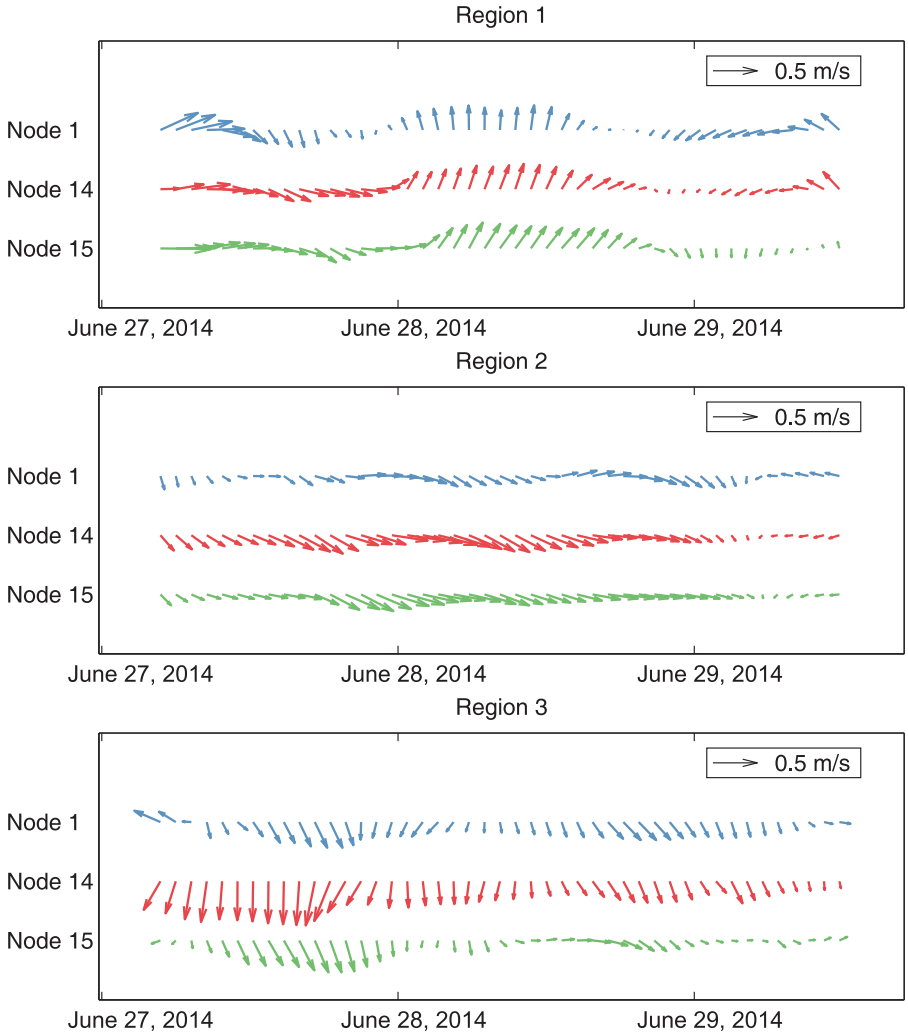

Fig. 7. The time variation of the current velocities in three positions (the locations of nodes 1, 14, and 15) for three different regions. The positions of the nodes and regions can be seen in Fig. 6.

as the true field is introduced. Then, we explain how to generate the measurement data. Following that, some simulation results of different estimation methods are compared and discussed.

A. Simulation Environment and Benchmark

The synthetic observational data are simulated based on a widely used community ocean model, ROMS [20]. ROMS is a primitive-equation ocean model that uses terrain-following coordinates and employs the hydrostatic pressure approximation.

A unified grid system with the horizontal resolution of 1 km is developed for part of the northwest region of the South China Sea. The model domain with 112×102 grid points is shown in Fig. 6, and the bathymetry is obtained by interpolating the 1 arc-minute global Earth Topography (ETOPO1) data set. Since the vertically integrated ocean current is considered in this study, only the barotropic solutions are calculated.

The initial and open boundary conditions of the model are generated from a global data assimilative ocean model, where the Hybrid Coordinate Ocean Model (HYCOM) is used as the dynamical model and the Navy Coupled Ocean Data Assimilation (NCODA) for data assimilation. The model is forced by the wind generated from the reanalysis data produced by the National Centers for Environmental Prediction (NCEP) Climate Forecast System Version 2 (CFSV2) [31]. The tidal forcing is also applied along the open boundaries. The time interval is set as 5 s to satisfy the typical Courant–Friedrichs–Lewy (CFL) condition.

In the simulations, $N_s = 19$ sensor nodes are deployed in the observation region, covering an area of 8 km $\times$ 8 km. The network topology is shown in Fig. 6, ensuring that the sensors are approximately uniformly distributed (per area). It is generated by the method proposed in [32]. In total, 42 reciprocal paths between neighboring nodes are produced, and the average distance is 2.15 km. The model was run for the period from 04:45:00 Z June 27, 2014 to 12:00:00 Z June 29, 2014, with a duration of around 55 h. In total, 222 time indexes of the current field are simulated and the time gap is 15 min.

Three different regions in the model domain are chosen to be studied. Fig. 7 shows the current velocities of some locations in

those regions. The velocities in nodes 1, 14, and 15 are displayed because they are located at the edge of the region and separated apart in space, indicating the velocity difference in space to some degree. The positions of those nodes can be seen in Fig. 6.

Fig. 8 shows the correlation coefficient of the synthetic data in time and space. The temporal correlation curve of all the grid points in space is averaged. For the spatial correlation curve, the positions from node 1 to node 19 are considered and the results are time averaged. It can be seen that the data show high correlation in time and space, and the curves decay with time or space. This result satisfies the model assumption in Sections III-C and III-D. Also, the spatial correlation curve in Fig. 8(b) is consistent with that in Fig. 3(b).

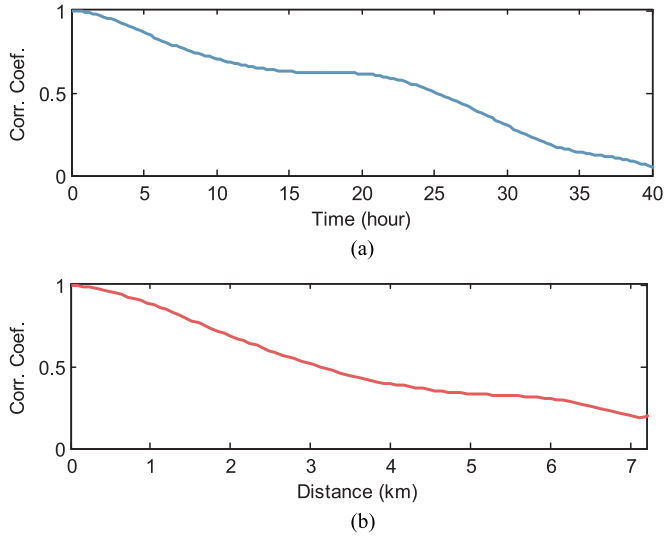

Fig. 8. The correlation coefficient curves of the synthetic data (region 1) with time and space. (a) Temporal correlation. (b) Spatial correlation.

B. Tomographic Reconstruction

After simulating the time-varying current field using ROMS, the next step is to find the travel time from one node to another to construct the measurement. One solution is to define a grid encompassing the tomographic region [33]. It is assumed that the velocity in each grid block is constant. If the grid is sparse, the discontinuous field may lead to an inaccurate estimation of travel time. The grid has to be dense enough to ensure the accuracy of the forward problem.

In this paper, we employ radial basis functions (RBFs) to reconstruct the smooth distribution and calculate the travel time measurement in the region. This idea is first proposed by Tabuchi *et al.* [34] for the reconstruction of a scalar field such as temperature, and it has been expanded to vector field [35]. It should be noticed that RBF is only used for calculating the travel time between any two locations in a current field, which is used as the measurement without error. It will not affect the proposed TE–KF and STE–KF methods. Next, we briefly review this method.

Rewriting (1), the travel time difference from positions $\mathbf{p}_i$ to $\mathbf{p}_j$ is

$$\Delta t_{\mathrm{ij}} = -\frac{\mathbf{v}_0 \cdot \mathbf{u}_{\mathrm{ij}}}{c_0^2} s_{\mathrm{ij}} - \int_{\mathbf{p}_i}^{\mathbf{p}_j} \left(\frac{\tilde{\mathbf{v}}(\mathbf{p}) \cdot \mathbf{u}_{\mathrm{ij}}}{c_0^2} \right) \mathrm{d}\mathbf{p} \tag{35}$$

where $\mathbf{v}_0$ is the mean value of current velocities in the field, and $\tilde{\mathbf{v}}(\mathbf{p}) = \mathbf{v}(\mathbf{p}) - \mathbf{v}_0$ is the velocity fluctuation at location $\mathbf{p}$. RBF networks are set up to reconstruct the velocity fluctuation $\tilde{\mathbf{v}}(\mathbf{p})$ in x- and y-directions, respectively.

An RBF network is a weighted sum of multiple RBFs which are nonlinear functions. Commonly used functions include Gaussian and polyharmonic splines. In the case of the Gaussian function, a single RBF can be expressed as

$$\Phi_{\mathbf{p}_c}(\mathbf{p}) = \exp\left(-k_r \|\mathbf{p} - \mathbf{p}_c\|^2\right) \tag{36}$$

where $\mathbf{p}_c$ is the location of the RBF center, and k_r is a scalar factor of the RBF. An RBF network is created from a linear combination of N_{RBF} RBFs with different centers. Denoting the velocity fluctuation $\tilde{\mathbf{v}}(\mathbf{p})$ in x-directions as an RBF network, we have

$$\tilde{v}^x(\mathbf{p}) = \sum_{j=1}^{N_{\mathrm{RBF}}} W_j^x \Phi_{\mathbf{p}_{cj}}(\mathbf{p}) = \mathbf{W}_x^T \mathbf{\Phi}(\mathbf{p}) \tag{37}$$

where $\mathbf{W}_x = [W_1^x, \ldots, W_{N_{\mathrm{RBF}}}^x]^T$ and $\mathbf{\Phi}(\mathbf{p}) = [\Phi_{\mathbf{p}_{c1}}(\mathbf{p}), \ldots, \Phi_{\mathbf{p}_{cN_{\mathrm{RBF}}}}(\mathbf{p})]^T$ are the vectors of weighting coefficients and RBFs, respectively. $\mathbf{W}_x$ is estimated using a least square method. The velocity fluctuation $\tilde{\mathbf{v}}(\mathbf{p})$ in y-directions can be formulated in a similar way. Then, (35) can be rewritten as

$$\Delta t_{\mathrm{ij}} = -\frac{\mathbf{v}_0 \cdot \mathbf{u}_{\mathrm{ij}}}{c_0^2} s_{\mathrm{ij}} - \int_{\mathbf{p}_i}^{\mathbf{p}_j} \left(\frac{\left[\mathbf{W}_x^T \mathbf{\Phi}(\mathbf{p}) \mathbf{u}_x + \mathbf{W}_y^T \mathbf{\Phi}(\mathbf{p}) \mathbf{u}_y\right] \cdot \mathbf{u}_{\mathrm{ij}}}{c_0^2} \right) \mathrm{d}\mathbf{p} \tag{38}$$

where $\mathbf{u}_x$ and $\mathbf{u}_y$ are the unit vectors in x- and y-directions, respectively.

Given a known horizontal current field, $\mathbf{v}(\mathbf{p}), \mathbf{v}_0$ and $\tilde{\mathbf{v}}(\mathbf{p})$ are easy to calculate. Then, $\mathbf{W}_x$ in (37) is estimated using a least square solution ($\mathbf{W}_y$ in a similar way). The travel time difference for each path in the network can be obtained with (38). A translated and rotated coordinate transformation can be applied to simplify the line integration in (38), which is described in [35].

In the simulations, considering the accuracy and computational complexity, $N_{\mathrm{RBF}} = 300$ RBF centers are uniformly distributed in the region, and the scalar factor is chosen as $k_r = 0.1\ \mathrm{km}^{-2}$.

C. Simulation Setup

We use region-averaged root-mean-square error (RMSE)

$$\mathrm{RMSE}(\hat{\mathbf{v}}_k) = \sqrt{\frac{1}{N_{\mathbf{p}}} \sum_{\mathbf{p} \in \mathcal{R}} \|\hat{\mathbf{v}}_k(\mathbf{p}) - \mathbf{v}_k(\mathbf{p})\|^2} \tag{39}$$

as the performance metric, where $\hat{\mathbf{v}}_k(\mathbf{p})$ is the estimate of the true value $\mathbf{v}_k(\mathbf{p})$ at location $\mathbf{p}$ and time k, and $N_{\mathbf{p}}$ is the number of velocity samples in the observation region $\mathcal{R}$.

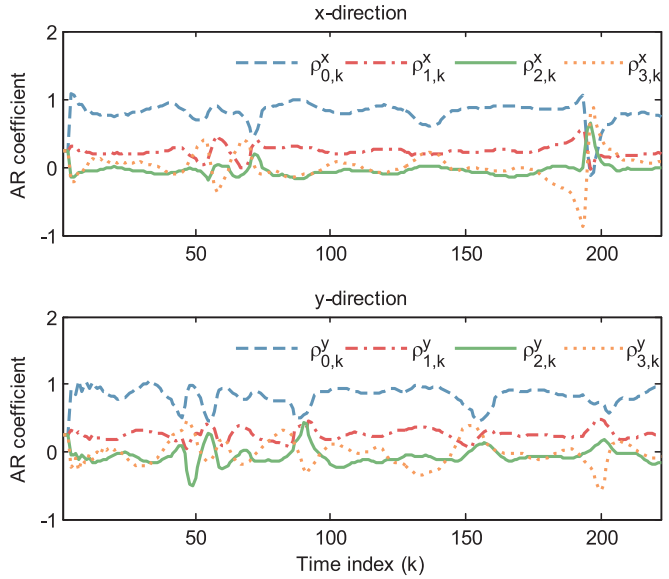

Fig. 9. Estimated AR coefficients of the synthetic data in region 1. The time gap of adjacent time indexes is 15 min.

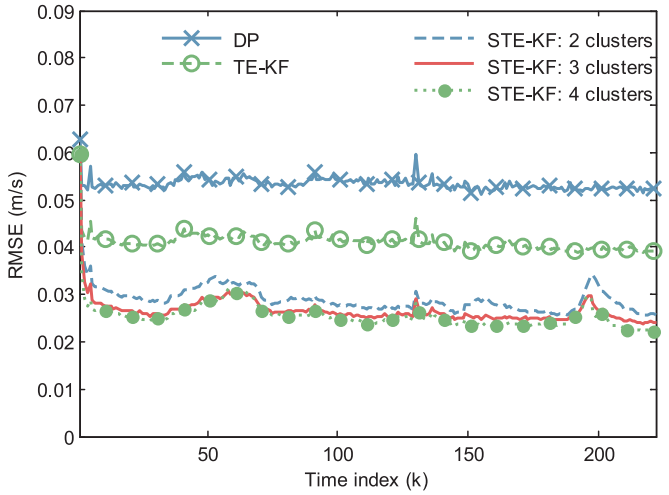

Fig. 10. Tracking performance of the STE–KF method with varying clusters versus the TE–KF and DP methods, where $\sigma_t = \sigma_0$. The time gap of adjacent time indexes is 15 min (region 1).

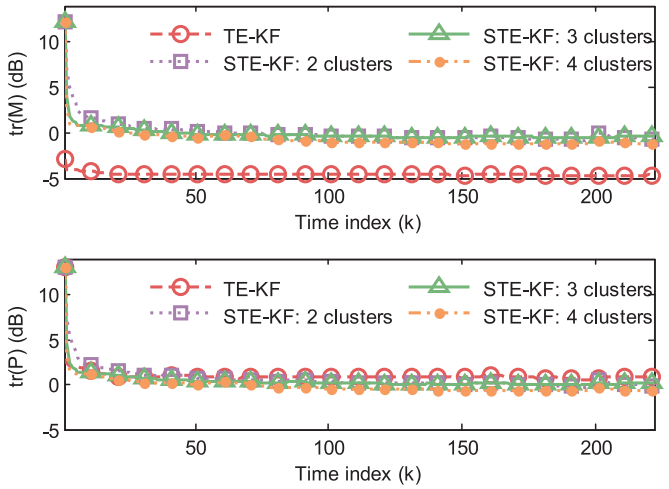

Fig. 11. The variance of $\mathrm{tr}(\mathbf{M}_k)$ and $\mathrm{tr}(\mathbf{P}_k)$ (in decibels) with time, where $\sigma_t = \sigma_0$. The time gap of adjacent time indexes is 15 min (region 1).

For practical consideration, a measurement error is added to the travel time of each path, which is assumed to be a Gaussian white noise with zero mean and variance σ_t^2. In the field experiment, a time-of-arrival measurement would be estimated from the peak of the cross correlation between the sent and received signals. The measurement noise increases as the SNR of the received signal decreases. Also, the received SNR depends on the transmission loss along the path for a specific source. Hence, the measurement error should be related to the distance between the node pairs. For the distributed network, the sensor nodes are nearly uniformly distributed in the region. For simplicity, we assume that the variances of measurement noise in all the paths are the same. Moreover, define $\sigma_0^2 = (0.055\,\mathrm{ms})^2$ as a reference value, which corresponds to 5% of the variance of time difference data. Measurement error σ_t can be expressed as a multiple of σ_0. The initial estimate is set to be the mean estimated current field at time $k = 1$. The past $K_{\mathrm{AR}} = 4$ states and the current state are used for updating the AR coefficients.

For the state–space model, the measurement noise can be determined by the measurement error and is assumed to be known in the simulations. The measurements are the travel time differences. Therefore, the measurement noise is set to be $\sigma_{\mathbf{n}_k} = \sigma_t/\sqrt{2}$. In reality, the SNR of the receiving signal can be a reference to the choice of $\sigma_{\mathbf{n}_k}$.

The state noise $\sigma_{\mathbf{w}_k}$ reflects the accuracy of the state transition model. If $\sigma_{\mathbf{w}_k}$ is too small, the tracking may diverge due to the model mismatch. If $\sigma_{\mathbf{w}_k}$ is too large, the effect of the state model becomes weak and the estimation results tend to be similar to those of the DP method. The state noise is generally estimated either using training data or assuming a spatiotemporal correlation.

In the simulations, the state noise is updated with the adaptive limited memory filter (ALMF) algorithm [36]. The ALMF algorithm is a noise estimator for adaptive correction of the *a priori* statistics which are intended to compensate for time-varying model errors. Specifically, the state noise for each velocity in the state vector is initialized as $\sigma_{\mathbf{w}_k} = 0.1$ m/s. The statistics of the state noise are updated at each time index with ALMF.

D. Simulation Results and Discussions

In this section, simulation results are given and discussed.

1) Performance of STE–KF: For the STE–KF method, we first show results of the AR coefficient estimation. Four clusters are included in the estimation. Fig. 9 shows the evolution of AR coefficients over time which are estimated from the synthetic data in region 1. The time-averaged AR coefficients are $\hat{\boldsymbol{\rho}}_{0,\mathrm{avg}} = [0.7995, 0.8204]$, $\hat{\boldsymbol{\rho}}_{1,\mathrm{avg}} = [0.2317, 0.2505]$, $\hat{\boldsymbol{\rho}}_{2,\mathrm{avg}} = [-0.0401, -0.0656]$ and $\hat{\boldsymbol{\rho}}_{3,\mathrm{avg}} = [0.0101, -0.0172]$, respectively. The simulation results indicate that the spatial correlation decreases as the distance increases.

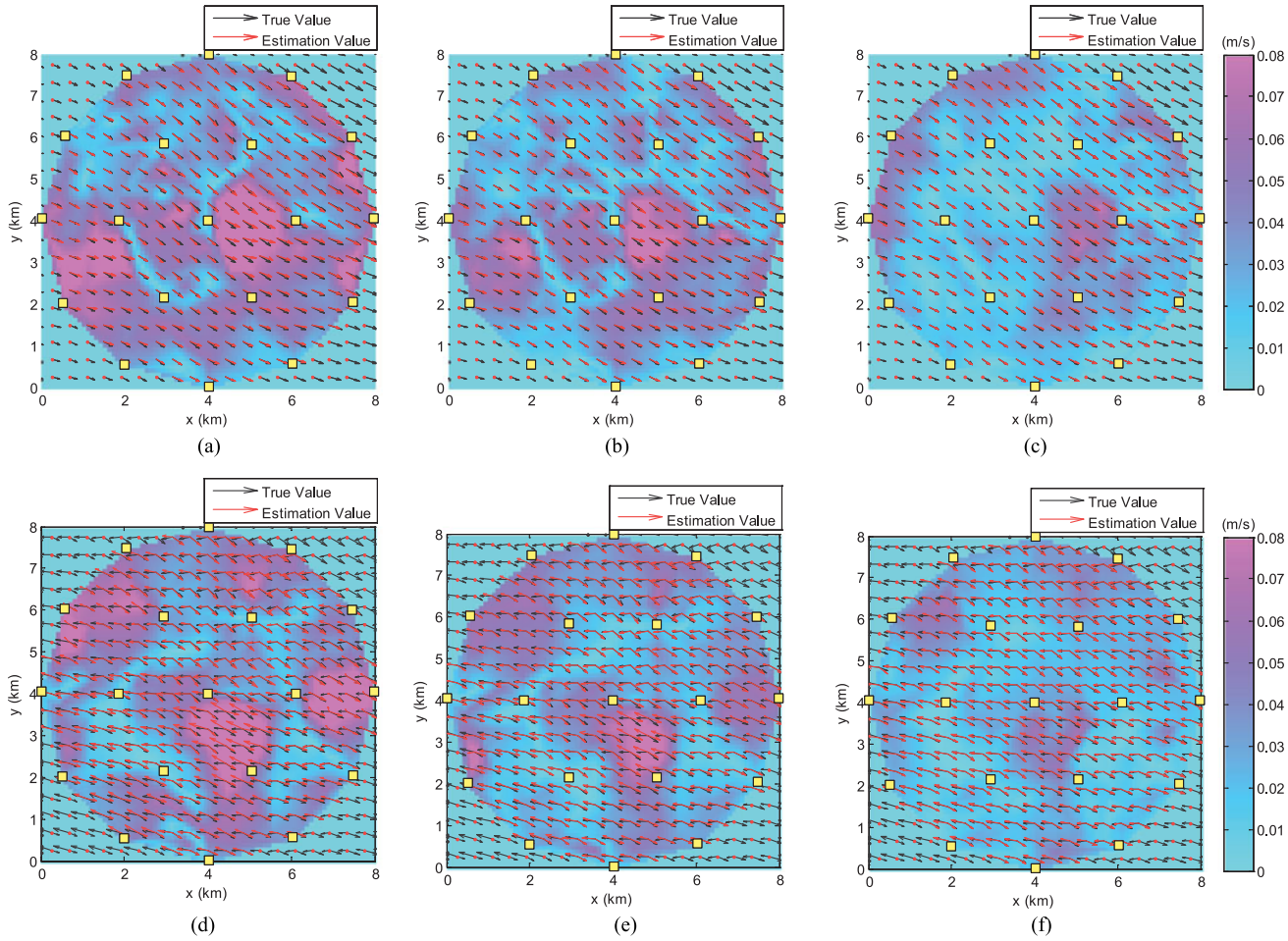

Fig. 12. Comparison of the estimated current velocities and true values at (a)–(c) $k = 50$ and (d)–(f) $k = 220$, where $\sigma_t = \sigma_0$. The color bar indicates the estimation error. The pink color refers to a higher value of the estimation error, while the light blue color refers to a lower value of the estimation error. (a) DP method, RMSE($\hat{\mathbf{v}}_{50}$) = 0.0530 m/s. (b) TE–KF method, RMSE($\hat{\mathbf{v}}_{50}$) = 0.0412 m/s. (c) STE–KF method with three clusters, RMSE($\hat{\mathbf{v}}_{50}$) = 0.0270 m/s. (d) DP method, RMSE($\hat{\mathbf{v}}_{220}$) = 0.0489 m/s. (e) TE–KF method, RMSE($\hat{\mathbf{v}}_{220}$) = 0.0378 m/s. (f) STE–KF method with three clusters, RMSE($\hat{\mathbf{v}}_{220}$) = 0.0261 m/s.

TABLE I
TIME-AVERAGED RMSES IN THREE REGIONS (IN METERS PER SECOND), WHERE $\sigma_t = \sigma_0$

Method	Region 1	Region 2	Region 3
DP	0.0534	0.0549	0.0559
TE-KF	0.0409	0.0431	0.0435
STE-KF: 2 clusters	0.0291	0.0316	0.0317
STE-KF: 3 clusters	0.0266	0.0292	0.0301
STE-KF: 4 clusters	0.0255	0.0291	0.0301

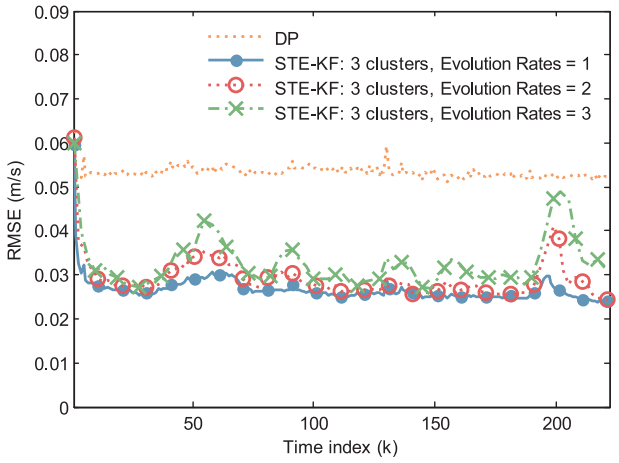

Fig. 13. Tracking performance for the current fields with different evolution rates, where $\sigma_t = \sigma_0$. The time gap of adjacent time indexes is 15 min (region 1).

Moreover, the AR coefficients are time varying, which means an update of AR coefficients is necessary during the tracking process.

Fig. 10 shows the tracking performance of the STE–KF method with different numbers of clusters in region 1, where $\sigma_t = \sigma_0$. The results are averaged over 100 independent experiments. The initial AR coefficients are set to be equal, and the sum equals to 1. For example, for the case of three clusters, $\mathbf{\Lambda}^{\rho}_{0,k} = \mathbf{\Lambda}^{\rho}_{1,k} = \mathbf{\Lambda}^{\rho}_{2,k} = (1/3)\mathbf{I}$ for $k \leq K_{\mathrm{AR}}$. From $k = K_{\mathrm{AR}} + 1$, AR coefficients are updated for each time index.

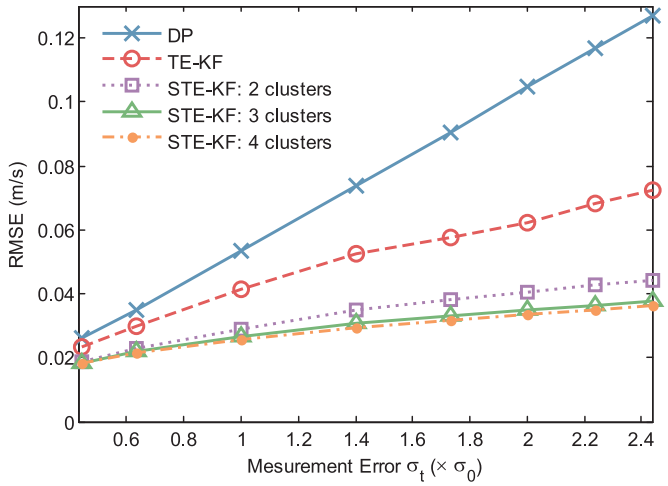

Fig. 14. Estimation results for different measurement errors (region 1).

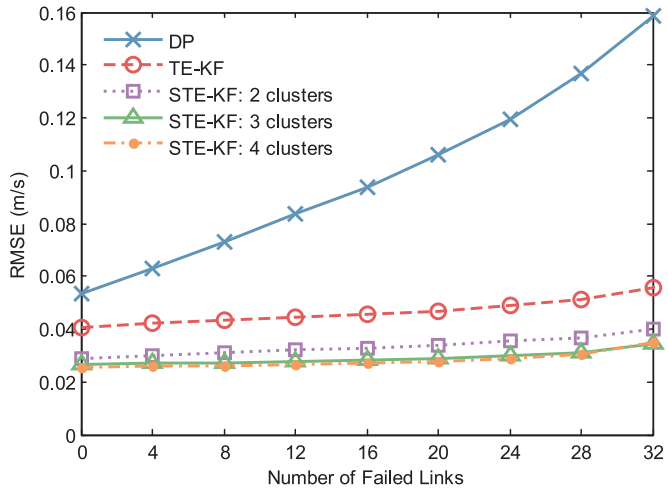

Fig. 15. The impact of random link failure on the estimation performance, where $\sigma_t = \sigma_0$ (region 1).

From Fig. 10, we observe that both TE–KF and STE–KF methods can track the variance after around ten time indexes. The estimation error of the STE–KF method is smaller than the TE–KF method. Moreover, the STE–KF method with three or four clusters shows a similar estimation curve, and slightly better performance than the case with two clusters. It indicates that the performance improves as the covered region of the spatial correlation model extends. However, when the spatial correlation region extends to some degree, the improvement of estimation performance is minor. This is because the spatial correlation degrades as the distance increases. When the distance is large enough, the correlation becomes very weak and no longer to be included.

Fig. 11 shows traces of error covariance matrices $\mathrm{tr}(\mathbf{M}_k)$ and $\mathrm{tr}(\mathbf{P}_k)$ of different tracking methods. It is seen that both $\mathrm{tr}(\mathbf{M}_k)$ and $\mathrm{tr}(\mathbf{P}_k)$ decrease with time and the curves converge to a steady state for both TE–KF and STE–KF methods.

2) Comparison of Different Methods: Fig. 12 compares the estimated current velocities and true values for different methods at time $k = 50$ and $k = 220$, where $\sigma_t = \sigma_0$. Since the measurement noise of each path is independent of time and space, the large estimation errors occur in different areas at time $k = 50$ and $k = 220$. For the DP method, the estimation performance is severely affected by the measurement error. The path with a large measurement error will lead to a large velocity bias in the area around the path. The TE–KF method can achieve a lower estimation error almost everywhere in the region than the DP method, while the estimation performance is still related to the measurement error. Comparatively, the estimation performance of the STE–KF method is better than the other two methods, and the effect of the high measurement error on STE–KF is very weak.

3) Different Regions: To verify the tracking performance in different environments, the simulations are performed in three regions depicted in Fig. 6. The current field variations are different in three regions, as shown in Fig. 7. Table I shows the time-averaged RMSEs in those regions, where $\sigma_t = \sigma_0$. Due to different spatial current distribution and change rate, the RMSEs differ slightly in three regions. However, the STE–KF method outperforms both TE–KF and DP methods in all three cases.

4) Different Evolution Rates: To investigate the effect of current evolution rate on tracking performance, we select one synthetic current field every two or three time indexes to form a new time-varying current field with a faster evolution rate. Fig. 13 shows the tracking curves for evolution rates 1, 2, and 3 of region 1, where $\sigma_t = \sigma_0$. As the evolution rate increases, the current field varies faster, and the performance degrades slightly. Although the errors for some time indexes increase, the curves tend to be stable in all three cases.

Further, the results in Fig. 13 show that, although the evolution rate increases, the STE–KF still performs better than DP. That means that in the field experiment, it is feasible to increase the measurement period for the STE–KF method, which can reduce the energy consumption.

5) Varying Measurement Errors: Fig. 14 shows the impact of the measurement error on the estimation performance. The difference of the RMSEs is not obvious when the measurement noise is low. It is because in that case, the measurement is trustable and a more complex state model makes limited contribution to the performance improvement. As σ_t increases, the TE–KF and STE–KF methods show their superiority compared with the DP method. Moreover, the STE–KF method with a larger number of clusters can achieve a slightly better performance.

6) Link Failure: In this simulation, we first assume that link failures randomly occur in all the travel paths with equal probability. For the DP method, when a failed link is detected, the velocities of related subtriangles are not estimated initially. After the velocities in the other regions are estimated, the velocities of these subtriangles can be obtained by a linear interpolation method. For the TE–KF and STE–KF methods, when a failed link is detected, the measurement noise of the corresponding measurement is set to be a large value, which means that this measurement is unacceptable.

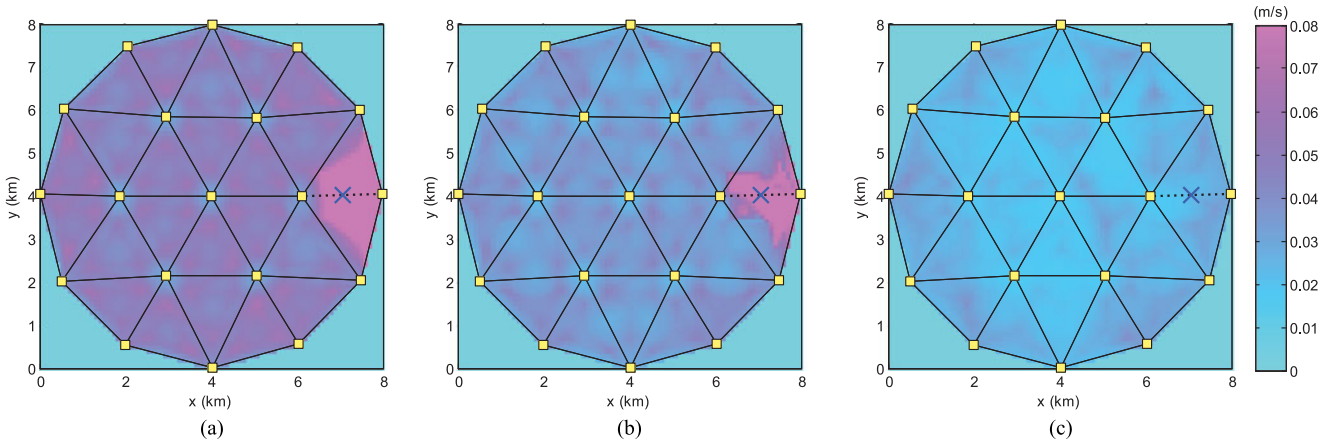

Fig. 16. Comparison of the time-averaged estimation error in the region when link failure occurs, where the link between nodes 16 and 19 is disconnected (marked with "x"), and $\sigma_t = \sigma_0$ (region 1). The color bar indicates the estimation error. The pink color refers to a higher value of the estimation error, while the light blue color refers to a lower value of the estimation error. (a) DP method. (b) TE–KF method. (c) STE–KF method with three clusters.

Fig. 15 compares the performance versus the number of failed links, where $\sigma_t = \sigma_0$. As the number of failed links increases, the estimation error of the DP method increases, while the TE–KF and STE–KF methods keep the estimation error almost constant. For the TE–KF method, the increase of RMSE is slightly higher than that of the STE–KF method. This reveals the fact that the spatiotemporal tracking method is robust to link failures. Indeed, the spatiotemporal evolution can compensate for the link failure via the state transition.

Next we consider the situation when a fixed link is broken. When the failed link is located at the central part of the region, the effect on the estimation is not obvious because the linear interpolation can compensate for the unobserved area. Hence, we only discuss the case where the failed link is near the boundary. Fig. 16 compares the time-averaged estimation error in the region when a specific link fails all the time, where the failure occurs between nodes 16 and 19. The DP and TE–KF methods both display large errors around the disconnected link, while the estimation error of the STE–KF method stays almost the same in this situation.

7) Burst Error: The burst error is modeled as an increase of the measurement noise in simulations. In the first simulation, burst errors are added to one or more random travel paths in specific time. At time $k = 50, 100$, and 150, burst errors in 1, 2, and 3 random links are, respectively, added with the measurement noise $10\sigma_t$. The burst errors are not detected by the system.

Fig. 17 shows the tracking performance of the different methods when burst errors occur at specific times. It can be seen that DP is obviously affected by the burst error. At time $k = 150$, the RMSE of DP increases from around 0.053 to 0.11, while for TE–KF and STE–KF, the RMSEs increase from around 0.04 to 0.076 and from around 0.027 to 0.045, respectively. It means that STE–KF can handle the situation of the sudden burst error better than the other two methods.

In the next simulation, the burst errors are added to one or more travel paths randomly. The measurement error of the burst error ranges from σ_t to $9\sigma_t$ in the simulations. Fig. 18 shows

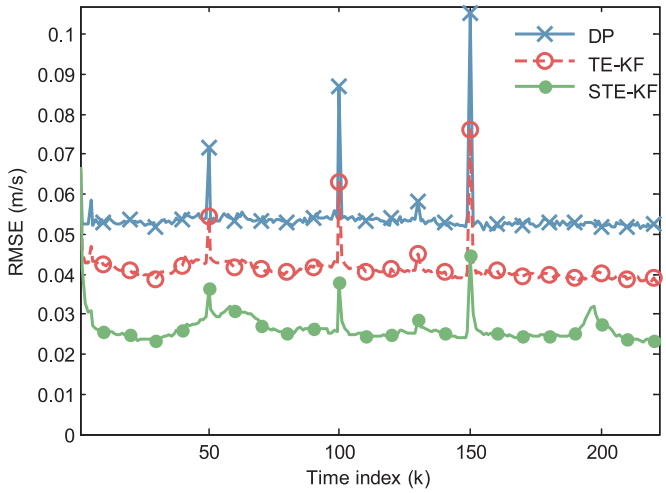

Fig. 17. Tracking performance of DP, TE–KF, and STE–KF with three clusters when burst errors occur at time $k = 50, 100$, and 150, with one, two, and three random error links, respectively, where $\sigma_t = \sigma_0$. The measurement error of burst errors is $10\sigma_t$. The time gap of adjacent time indexes is 15 min (region 1).

the estimation results for different noise levels σ_e of burst errors, where $\sigma_t = \sigma_0$. For TE–KF and STE–KF, we consider two situations: the burst error is detected by the system or it is not detected by the system. If the system detects the error, the measurement noise of the corresponding measurement is set as a new value based on the level of the burst error. If not detected, the measurement noise level stays the same.

In Fig. 18(a), the slopes of the curves for the three methods are similar when the error links are not detected. It is because the error links are regarded as a measurement with small error for TE–KF and STE–KF, which results in model mismatch. However, if the error links are detected and the error level is known by the system, as shown in Fig. 18(b), the RMSEs of the TE–KF and STE–KF methods both do not vary too much as the error level increases. It indicates that the performance of the

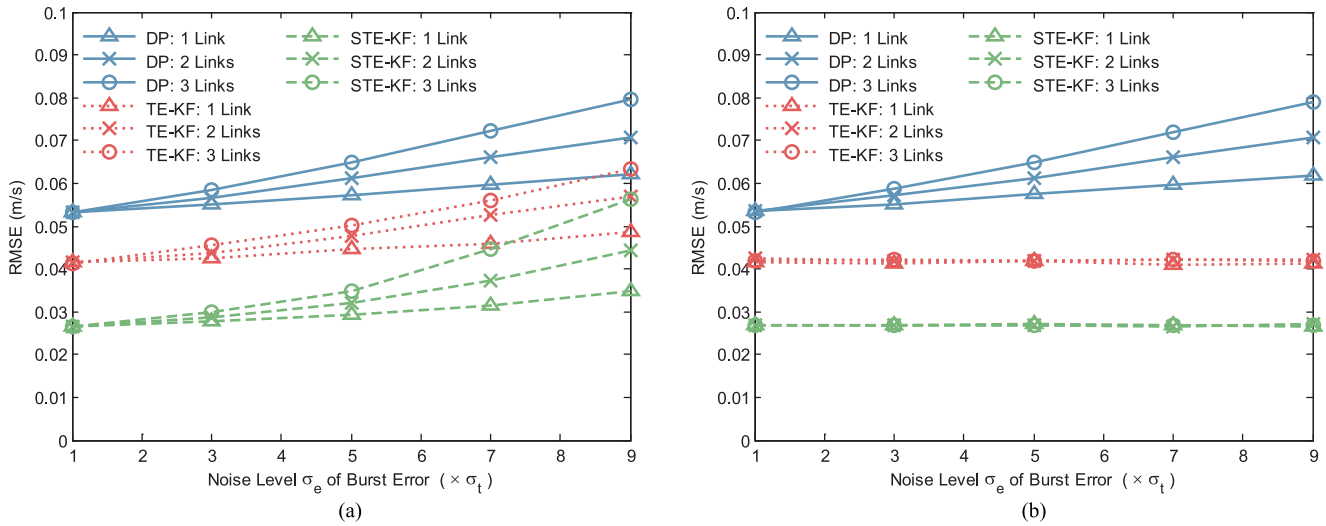

Fig. 18. The estimation results for different situations of burst errors, where $\sigma_t = \sigma_0$ (region 1). The error links are (a) not detected or (b) detected by the system. The STE–KF method with three clusters is used for comparison. "# Link(s)" is the number of random burst error links.

TE–KF and STE–KF methods is not affected when one or more links experience burst errors and the error links are captured by the system.

V. Conclusion

The DNUS system is an emerging technology due to its great potential in underwater applications. In this paper, horizontal ocean current field tracking with a DNUS system was investigated. The tracking approach utilizes the physical evolving characteristics of the current field in time and space. First, a temporal evolution tracking model of the current field was proposed by modeling the evolution of the velocity in each subtriangle as a first-order AR process. Then, we proposed a spatiotemporal tracking model, which makes use of the spatiotemporal correlation of the current field. The spatiotemporal AR model can adapt well with the variance of the current field by updating AR coefficients over time.

A synthetic data set generated by ROMS was used to evaluate the performance of the proposed method. The simulation results show that the proposed TE–KF and STE–KF methods are capable of tracking the variance of the current field in different observation regions, with different measurement errors or current evolution rates. The STE–KF method can achieve a better performance than the TE–KF method by incorporating the spatiotemporal correlation; its performance improves as the covered region of spatial correlation model extends. Moreover, the impact of link failure or burst errors was discussed. It was found that TE–KF can deal with the cases of random link failure and burst errors if observed by the system, while it cannot perform well when a fixed link near the boundary is broken. Comparatively, STE–KF was shown to be resistant to both random and fixed link failures. Overall the proposed method is robust to various practical underwater problems.

In our method, observations are gathered by a fusion center for centralized processing. The communication cost is large and should be considered in the practical scenario. By contrast, decentralized strategies require less communication and allow parallel processing in a collaborate manner. We will focus on a distributed implementation of the proposed method in the future research.

References

[1] A. Joseph, "Horizontally integrated remote measurements of ocean currents using acoustic tomography techniques," in *Measuring Ocean Currents*, A. Joseph, Eds. Boston, MA, USA: Elsevier, 2014, Ch. 7, pp. 201–239.

[2] W. Munk and C. Wunsch, "Ocean acoustic tomography: A scheme for large scale monitoring," *Deep-Sea Res.*, vol. 26, no. 2, pp. 123–161, 1979.

[3] R. Spindel *et al.*, "Acoustic tomography for monitoring the Sea of Japan: A pilot experiment," *IEEE J. Ocean. Eng.*, vol. 28, no. 2, pp. 297–302, Apr. 2003.

[4] I. Iturbe, P. Roux, B. Nicolas, J. Virieux, and J. Mars, "Shallow-water acoustic tomography performed from a double-beamforming algorithm: Simulation results," *IEEE J. Ocean. Eng.*, vol. 34, no. 2, pp. 140–149, Apr. 2009.

[5] X.-H. Zhu *et al.*, "Mapping tidal current structures in Zhitouyang Bay, China, using coastal acoustic tomography," *IEEE J. Ocean. Eng.*, vol. 38, no. 2, pp. 285–296, Apr. 2013.

[6] H. Yamaoka *et al.*, "Coastal acoustic tomography system and its field application," *IEEE J. Ocean. Eng.*, vol. 27, no. 2, pp. 283–295, Apr. 2002.

[7] J. Lin, A. Kaneko, N. Gohda, and K. Yamaguchi, "Accurate imaging and prediction of Kanmon Strait tidal current structures by the coastal acoustic tomography data," *Geophys. Res. Lett.*, vol. 32, no. 14, pp. 1–4, 2005.

[8] C.-F. Huang, T. C. Yang, J.-Y. Liu, and J. Schindall, "Acoustic mapping of ocean currents using networked distributed sensors," *J. Acoust. Soc. Amer.*, vol. 134, no. 3, pp. 2090–2105, 2013.

[9] I. F. Akyildiz, D. Pompili, and T. Melodia, "Underwater acoustic sensor networks: research challenges," *Ad Hoc Netw.*, vol. 3, no. 3, pp. 257–279, 2005.

[10] T. C. Yang, "Distributed underwater sensing: A paradigm change for the future," in *Advanced Materials*, S.-H. Chang, A. I. Parinov, and Y. V. Topolov, Eds., Switzerland: Springer International Publishing, 2014, Ch. 21, pp. 261–275.

[11] J. K. Hart and K. Martinez, "Environmental sensor networks: A revolution in the earth system science?" *Earth-Sci. Rev.*, vol. 78, no. 3, pp. 177–191, 2006.

[12] A. Goodney and Y. H. Cho, "Water temperature sensing with microtomography," *Int. J. Sens. Netw.*, vol. 12, no. 2, pp. 65–77, 2012.

[13] C. L. Lawson and R. J. Hanson, *Solving Least Squares Problems*, Englewood Cliffs, NJ, USA: Prentice-Hall, 1974, Ch. 23.

[14] M. Ghil and P. Malanotte-Rizzoli, "Data assimilation in meteorology and oceanography," *Adv. Geophys.*, vol. 33, pp. 141–266, 1991.
[15] J.-H. Park and A. Kaneko, "Assimilation of coastal acoustic tomography data into a barotropic ocean model," *Geophys. Res. Lett.*, vol. 27, no. 20, pp. 3373–3376, 2000.
[16] B. M. Howe, K. Runciman, and J. A. Secan, "Tomography of the ionosphere: Four-dimensional simulations," *Radio Sci.*, vol. 33, no. 1, pp. 109–128, 1998.
[17] B. M. Howe, "Ocean acoustic tomography: Mesoscale velocity," Ph.D. dissertation, Univ. California San Diego, La Jolla, CA, USA, 1986.
[18] R. L. Martin and J. Oeppen, "The identification of regional forecasting models using space-time correlation functions," *Trans. Inst. Br. Geogr.*, no. 66, pp. 95–118, 1975.
[19] S. Kolouri, M. R. Azimi-Sadjadi, and A. Ziemann, "Acoustic tomography of the atmosphere using unscented Kalman filter," *IEEE Trans. Geosci. Remote Sens.*, vol. 52, no. 4, pp. 2159–2171, Apr. 2014.
[20] A. F. Shchepetkin and J. C. McWilliams, "The regional oceanic modeling system (ROMS): A split-explicit, free-surface, topography-following-coordinate oceanic model," *Ocean Model.*, vol. 9, no. 4, pp. 347–404, 2005.
[21] B. M. Howe, P. F. Worcester, and R. C. Spindel, "Ocean acoustic tomography: Mesoscale velocity," *J. Geophys. Res.*, vol. 92, no. C4, pp. 3785–3805, 1987.
[22] F. Gaillard, "Evaluating the information content of tomographic data: Application to mesoscale observations," *J. Geophys. Res.*, vol. 97, no. C10, pp. 15489–15505, 1992.
[23] C. Yardim, Z.-H. Michalopoulou, and P. Gerstoft, "An overview of sequential Bayesian filtering in ocean acoustics," *IEEE J. Ocean. Eng.*, vol. 36, no. 1, pp. 71–89, Jan. 2011.
[24] Y. Zhang, J. Huang, H. Zhao, and W. Xu, "Kalman tracking of ocean current field based on distributed sensor network," in *Proc. OCEANS Conf.*, 2014, DOI: 10.1109/OCEANS.2014.7003157.
[25] K. Mizumura, "Applications of Kalman filter to oceanic data," *J. Waterw. Port Coast. Ocean Eng.*, vol. 110, no. 3, pp. 334–343, 1984.
[26] W. W.-S. Wei, *Time Series Analysis: Univariate and Multivariate Methods*, Redwood City, CA, USA: Addison-Wesley, 1994, Ch. 3.
[27] D. Tritton, *Physical Fluid Dynamics*, Oxford, U.K.: Clarendon, 1988, Ch. 20.
[28] M. P. Paidoussis, *Fluid-Structure Interactions: Slender Structures and Axial Flow*, Cambridge, MA, USA: Academic, 1998, Ch. 2.
[29] P. E. Pfeifer and S. J. Deutsch, "A three-stage iterative procedure for space-time modeling," *Technometrics*, vol. 22, no. 1, pp. 35–47, 1980.
[30] A. Tikhonov and V. Arsenin, *Solutions of Ill-Posed Problems*, Ser. Scripta Series in Mathematics, Washington, DC, USA: Winston & Sons, 1977, Ch. 3.
[31] S. Saha *et al.*, "The NCEP climate forecast system version 2," *J. Climate*, vol. 27, no. 6, pp. 2185–2208, 2014.
[32] P.-O. Persson and G. Strang, "A simple mesh generator in MATLAB," *SIAM Rev.*, vol. 46, no. 2, pp. 329–345, 2004.
[33] D. K. Wilson and D. W. Thomson, "Acoustic tomographic monitoring of the atmospheric surface layer," *J. Atmos. Ocean. Technol.*, vol. 11, no. 3, pp. 751–769, 1994.
[34] H. Tabuchi, T. Miyoshi, H. Ichibashi, and K. Ohno, "Computerized tomography with radial basis functions network: A neuro-fuzzy approach," in *Proc. IEEE Int. Conf. Neural Netw.*, 1995, pp. 2258–2263.
[35] T. Wiens, "Sensing of turbulent flows using real-time acoustic tomography," in *Proc. 19th Biennial Conf. New Zealand Acoust. Soc.*, 2008.
[36] K. Myers and B. D. Tapley, "Adaptive sequential estimation with unknown noise statistics," *IEEE Trans. Autom. Control*, vol. 21, no. 4, pp. 520–523, Aug. 1976.

Ying Zhang received the B.S. degree in information and communication engineering from Zhejiang University, Hangzhou, China, in 2010, where he is currently working toward the Ph.D. degree at the College of Information Science and Electronic Engineering.

His research interests include signal processing, ocean acoustic tomography, underwater sensor network, and underwater acoustic communication.

Huifang Chen (M'99) received the B.S. degree in electronic engineering, the M.S. degree in communication and electronic systems, and the Ph.D. degree in communications and information systems from Zhejiang University, Hangzhou, China, in 1994, 1997, and 2000, respectively.

Since 2000, she has been with Zhejiang University where she is now an Associate Professor in the College of Information Science and Electronic Engineering. From 2005 to 2007, she worked as a Postdoctoral Researcher supported by the Japanese Government MEXT Scholarship in the Department of Computer Science, Shizuoka University, Hamamatsu, Japan. Her research interests include wireless networks, underwater acoustic networks, integrated communications and signal processing, and wireless network security.

Wen Xu (SM'04) received the B.E. degree in electrical engineering from the University of Science and Technology of China, Hefei, China, in 1990, the M.S. degree in acoustics from the Institute of Acoustics, Chinese Academy of Sciences, Beijing, China, in 1993, and the Ph.D. degree in oceanographic engineering from the Massachusetts Institute of Technology (MIT), Cambridge, MA, USA, in 2001.

From 1993 to 1996, he was a Research Engineer with the Institute of Acoustics, Chinese Academy of Sciences. He was with the Ocean Acoustics Group, MIT, as a Research Scientist from 2001 to 2002, and with the Teledyne RD Instruments, San Diego, CA, USA, as a Research Scientist/Senior Research Scientist from 2003 to 2007. Currently, he is a Professor at the College of Information Science and Electronic Engineering, Zhejiang University, Hangzhou, China. His research has concerned statistical and array signal processing in general and in applications to sonar, radar, and communication systems, and most recently to underwater sensor network.

T. C. Yang received the Ph.D. degree in high energy physics from the University of Rochester, Rochester, NY, USA, in 1971.

He is currently a full professor at the College of Information Science and Electronic Engineering, Zhejiang University, Hangzhou, China. From 2012 to 2014, he was a National Science Counsel Chair Professor at the Institute of Applied Marine Physics and Undersea Technology, College of Marine Science, National Sun Yat-Sen University, Kaohsiung, Taiwan. Before that, he spent 32 years working at the Naval Research Laboratory, Washington, DC, USA, serving as Head of the Arctic Section, Dispersive Wave Guide Effects Group, and acting Head of the Acoustic Signal Processing Branch, and consultant to the division on research proposals. His current research focuses on: 1) environmental impacts on underwater acoustic communications and networking, exploiting the channel physics to characterize and improve performance; and 2) environmental acoustic sensing and signal processing issues aimed at improving the effectiveness of distributed networked sensing. In earlier years, he pioneered matched mode processing for a vertical line array, and matched-beam processing for a horizontal line array. Other areas of research included geoacoustic inversions, waveguide invariants, effects of internal waves on sound propagation in shallow water, Arctic acoustics, etc.

Prof. Yang is a Fellow of the Acoustical Society of America.

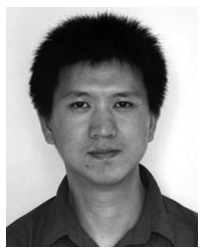

Jiamin Huang received the B.S. and Ph.D. degrees in solid mechanics from Zhejiang University, Hangzhou, China, in 2007 and 2012, respectively.

He was a Postdoctoral Researcher in the College of Information Science and Electrical Engineering, Zhejiang University, Hangzhou, China, from 2012 to 2014. Currently, he is an Assistant Researcher in the College of Information Science and Electrical Engineering, Zhejiang University. His main research interests lie in the areas of ocean modeling, underwater acoustics and data assimilation.